Chemical Engineering Science 249 (2022) 117356

Contents lists available at ScienceDirect

Chemical Engineering Science

journal homepage: www.elsevier.com/locate/ces

Modeling of temperature swing adsorption-oxidation of volatile organic compounds

Busuyi O. Adebayo, Fateme Rezaei *

Department of Chemical & Biochemical Engineering, Missouri University of Science and Technology, 1101 N State Street, Rolla, MO 65409, United States

HIGHLIGHTS

- Simulation of a temperature swing adsorption-oxidation (TSAO) process for VOCs abatement.
- Effects of VOC feed concentration, temperature, flow rate, and step times are analyzed.
- Model predictions are compared with experimental data.
- Parametric analysis is carried out to assess the impacts of process conditions on key performance indicators.

GRAPHICAL ABSTRACT

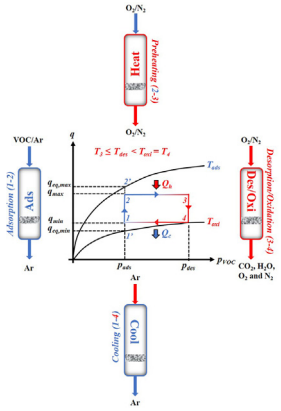

ARTICLE INFO

Article history:
Received 28 May 2021
Received in revised form 10 October 2021
Accepted 6 December 2021
Available online 10 December 2021

Keywords:
TSAO
Numerical modeling
VOC
Removal efficiency
Process performance

ABSTRACT

In this work, we simulated a single-bed 4-step temperature swing adsorption-oxidation (TSAO) process for capture and *in situ* oxidation of benzene, as a model VOC, over Ni/ZrO_2-SiO_2, as a dual-function material (DFM). The TSAO cycles consisted of adsorption, preheating, desorption/oxidation, and cooling steps. The model sensitive parameters were estimated via parameter estimation and validated against experimental data. Extensive parametric analysis was carried out to investigate the effects of key process variables on the TSAO performance. Model results revealed relatively good prediction of the process. Under the conditions investigated, adsorption, oxidation and total removal efficiencies were estimated to be 76, 84 and 66%, respectively. It was also established that the proposed 4-step cyclic TSAO could be reduced to a 3-step TSAO process consisting of adsorption, heating/desorption/oxidation, and cooling steps without any loss in performance. Finally, it was demonstrated that indirect convective cooling is far superior to direct feed cooling.

1. Introduction

Volatile organic compounds (VOCs) are a harmful class of toxic industrial chemicals that are detrimental to human health and the environment. In the atmosphere, VOCs can react with nitrogen oxides (NO_x) to form ozone (O_3) under the influence of sunlight and also with secondary aerosol to form particulate matters which are also highly toxic (Gelles et al., 2020). VOCs in the upper atmosphere cause stratospheric ozone layer depletion which leads to greenhouse effect and thus global warming. Increasing environmental awareness coupled with strong public outcry has led to

* Corresponding author.
E-mail address: rezaeif@mst.edu (F. Rezaei).

https://doi.org/10.1016/j.ces.2021.117356
0009-2509/

Nomenclature

A_B	Bed surface area per volume of bed [1/m]
A_{pa}	Surface area of particles per volume of bed [m^2 particles/m^3 bed]
A_x	Bed interstitial cross-sectional area ($=\varepsilon_b \pi r_B^2$), [m^2]
A_{VOC}	Surface reduction of benzene Arrhenius constant (5.35×10^{10} m^3/kg/s)
A_{O2}	Surface reoxidation of O_2 Arrhenius constant (3.45×10^7 m^3/kg/s)
c_b	Bulk gas component concentration, [mol/m^3]
c_p	Gas concentration in the pores, [mol/m^3]
c	Total bulk gas concentration, [mol/m^3]
c_0	Initial concentration, [mol/m^3]
$c_{f,ads}$	Feed concentration during adsorption, [mol/m^3]
$c_{f,pht}$	Feed concentration during preheating, [mol/m^3]
$c_{f,deo}$	Feed concentration during desorption/oxidation, [mol/m^3]
$c_{f,cool}$	Feed concentration during cooling, [mol/m^3]
$\hat{c}$	Specific heat capacity, [J/kg/K]
d_{int}	Column internal diameter, [m]
d_{ext}	Column external diameter, [m]
d_B	Bed diameter ($\approx d_{int}$), [m]
d_{pa}	Particle diameter, [m]
D_{ax}	Axial dispersion coefficient, [m^2/s]
$D_{eff,p}$	Intraparticle effective pore diffusivity, [m^2/s]
$D_{eff,K,p}$	Intraparticle effective Knudsen diffusivity, [m^2/s]
$D_{eff,m,p}$	Intraparticle effective molecular diffusivity, [m^2/s]
$D_{K,p}$	Intraparticle Knudsen diffusivity, [m^2/s]
$D_{m,p}$	Intraparticle molecular diffusivity, [m^2/s]
D_m	Interparticle molecular diffusivity, [m^2/s]
$D_{m,ij}$	Intraparticle molecular binary diffusivity, [m^2/s]
E_{VOC}	Reaction activation energy with respect to the VOC (96,351 J/mol)
E_{O2}	Reaction activation energy with respect to O_2 (97,939 J/mol)
$\tilde{\tilde{E}}_a$	Total reaction activation energy, [J/mol]
E_{eir}	Energy input rate, [J/s]
E_{spe}	Specific energy consumption, [J/mol]
h_r	Heating rate, [1/s]
$h_{a,r}$	Ambient (furnace) heating rate, [1/s]
$h_{f,r}$	Inlet feed-furnace heat transfer rate in the column space above the bed, [1/s]
h_F	Film gas-particle average heat transfer coefficient, [W/m^2/K]
ΔH_{liq}	Enthalpy change of normal liquefaction/condensation, [J/mol]
ΔH_{sor}	Enthalpy change of sorption (adsorption or desorption) of the first layer, [J/mol]
$\Delta\tilde{\tilde{H}}_{sor}$	Total enthalpy change of sorption, [J/mol]
$\Delta\tilde{\tilde{H}}_{oxi}$	Total enthalpy change of oxidation, [J/mol]
k_F	Film mass transfer coefficients, [m/s]
k	Arbitrary process rate constant [Dimension is process-dependent]
k_{VOC}	Surface reduction rate constant of benzene, [1/s]
k_{O2}	Surface reoxidation rate constant of O_2, [1/s]
$\tilde{\tilde{K}}_{sor}$	Total rate of sorption [m/s]
$\tilde{\tilde{K}}_{oxi}$	Total rate of oxidation [1/s]
L	Bed height, [m]
L_c	Column height, [m]
m	Bed mass, i.e., mass of DFM sample loaded in the column, [kg]
$\tilde{\tilde{m}}_{b,g}$	Bulk gas total mass, [kg]
$\tilde{\tilde{m}}_{p,g}$	Particle pore gas total mass, [kg]
$\tilde{\tilde{m}}_{ads}$	Total mass adsorbed, [kg]
M	Molar mass, [kg/mol]
$\tilde{\tilde{n}}_{ads}$	Total mole adsorbed, [mol]
$\tilde{\tilde{n}}_{des}$	Total mole desorbed, [mol]
n and N	Number, [-]
N_{Nu}	Nusselt number, [-]
N_{Pe}	Péclet number, [-]
N_{Pr}	Prandtl's number, [-]
N_{Ra}	Rayleigh number, [-]
N_{Re}	Reynold's number, [-]
N_{Sh}	Sherwood number, [-]
P_b	Bulk gas total pressure, [Pa]
P_p	Particle pore gas total pressure, [Pa]
p_p	Particle pore gas partial pressure, [Pa]
q	Dynamic quantity adsorbed, [mol/kg]
q_{eq}	Equilibrium quantity adsorbed, [mol/kg]
$q_{eq,f}$	q_{eq} at the feed conditions, [mol/kg]
r	Particle radial distance coordinate
r_B	Bed radius ($=d_B/2$), [m]
r_{pa}	Particle radius ($=d_{pa}/2$), [m]
r_p	Particle mean pore radius, [m]
R_{sor}	Sorption rate (R_{ads} during adsorption and R_{des} during desorption), [mol/kg/s]
R_{oxi}	Oxidation rate, [mol/kg/s]
Stoic	Reaction component stoichiometric coefficient, [-]
t	Time coordinate, [s]
t_{ads}	Adsorption step period, [s]
t_{pht}	Preheating step period, [s]
t_{deo}	Desorption/oxidation step period, [s]
t_{cool}	Cooling step period, [s]
t_h	Column wall thickness ($=d_{ext} - d_{int}$), [m]
T_b	Bed bulk gas temperature, [K]
T_{pa}	Particle temperature, [K]
$\underline{T}_w$	Column wall temperature, [K]
T_w	Mean temperature of the column wall, [K]
T_a	Ambient (furnace) temperature, [K]
$T_{a,final}$	Ambient (furnace) final temperature during each step, [K]
T_f	Inlet feed temperature, [K]
$T_{f,final}$	Inlet feed final temperature during each step, [K]
T_{crit}	Benzene critical temperature (562.15 K)
$T_{a,final}$	Ambient (furnace) final temperature during each step, [K]
$T_{f,ads,0}$	Feed initial temperature during adsorption, [K]
$T_{f,pht,0}$	Feed initial temperature during preheating, [K]
$T_{f,deo,0}$	Feed initial temperature during desorption/oxidation, [K]
$T_{f,cool,0}$	Feed initial temperature during cooling, [K]
T_0	Bed initial temperature, [K]
T_{ads}	Adsorption temperature, [K]
T_{des}	Desorption temperature, [K]
T_{oxi}	Oxidation temperature, [K]
u	Bed interstitial axial velocity, [m/s]
v_{pa}	Particle specific pore volume, [m^3/kg]
V_B	Bed volume, [m^3]
$\dot{v}_{f,ads}$	Feed flow rate during adsorption, [mL/min]
$\dot{v}_{f,pht}$	Feed flow rate during preheating, [mL/min]
$\dot{v}_{f,deo}$	Feed flow rate during desorption/oxidation, [mL/min]
$\dot{v}_{f,cool}$	Feed flow rate during cooling, [mL/min]
w	DFM component weight fraction, [wt.%]
z	Bed axial distance coordinate, [m]

Greek Letters

α	Thermal difusivity, [m^2/s]
β	Thermal expansivity, [1/K]
ν	Kinematic viscosity, [m^2/s]

γ	Set of arbitrary parameters in the model	Ω_{ij}	Diffusional collision integral, [-]
ε_b	Bed bulk (interparticle) porosity, [-]	μ_g	Gas dynamic viscosity, [kg/m/s]
ε_{pa}	Particle porosity (bed intraparticle porosity), [-]	δ_p	Particle pore constrictivity, [-]
κ_a	Ambient/furnace gas thermal conductivity, [W/m/K]	τ_p	Particle pore tortuosity, [-]
κ_b	Bulk gas thermal conductivity, [W/m/K]	θ	Weight fraction of ZrO_2-SiO_2 in DFM, [-]
ρ_g	Gas density, [kg/m^3]	λ_{eff}	Thermal conductivity of the DFM, [W/m/K]
ρ_{pa}	Particle density, [kg/m^3]	$\lambda_{ZrO2\text{-}SiO2}$	Thermal conductivity of ZrO_2-SiO_2 support, [W/m/K]
ρ_s	Particle skeletal density, [kg/m^3]	λ_{Ni}	Thermal conductivity of Ni catalyst, [W/m/K]
σ_{ij}	Kinematic diameter, [m]		

strict regulations to control VOC emissions. Consequently, an abatement process with high cost-effectiveness, efficiency, and reliability is necessary for abating these harmful compounds. There are various techniques available for the abatement of VOCs, among which adsorption and thermal and catalytic oxidation have received universal acceptance (Krishnamurthy et al., 2020). Adsorption largely depends on stream VOCs' concentrations. At the usual low VOCs' concentrations, the adsorption capacity of most adsorbents is compromised. Thermal oxidation is undoubtedly one of the best techniques because of its high efficiency in fully destructing the VOCs, however, it requires a concentrated feed to be energy-efficient and thus be economically feasible. Catalytic oxidation on the other hand suffers from large catalyst inventory and rapid catalyst deactivation.

One way to overcome all these bottlenecks is to develop an integrated process where the dilute feed is concentrated over a porous adsorbent, followed by its subsequent oxidation over a catalyst material. In recent years, a commendable effort has gone into developing dual-function materials (DFMs) for sequential adsorption and reaction, and the experimental investigation of their performance (Kullavanijaya et al., 2000; Urbutis and Kitrys, 2014; Huang et al., 2009; Adebayo et al., 2020a; Adebayo et al., 2020c); however, little attention has been given to the numerical studies of the combined process. Thus, a fast, accurate, and robust numerical model that can predict the behavior of this integrated process is highly desirable. It should be noted that modeling of cyclic processes such as temperature or pressure swing adsorption (TSA or PSA) has been extensively investigated for various gas separation processes (Shivaji et al., 2012; Hosseinzadeh Hejazi et al., 2017; Pai et al., 2018; Lopes et al., 2011; Effendy et al., 2017; Xiao et al., 2012; Rezaei et al., 2014; Ntiamoah et al., 2015; Casas et al., 2013). In a study by Kolade et al. (2009) an adsorptive reactor for VOC abatement was numerically studied based on a two-step sequential adsorption and reactive regeneration process in a monolithic reactor, and the process performance was investigated against process key performance indicators (KPIs). However, neither experimental validation nor optimization was carried out to access the feasibility of this complex process. In other investigations, Campesi et al. (2012), Campesi et al. (2015) used a two-bed adsorber reactor system to concentrate a VOC-lean stream before catalytic oxidation, however, the modeling aspect was sparse.

In our prior works, (Adebayo et al., 2020a; Adebayo et al., 2020c) we developed a series of adsorbent-catalyst DFMs based on TiO_2-SiO_2, ZrO_2-SiO_2, and Ni/ZrO_2-SiO_2 for abatement of aromatic VOCs including benzene and toluene, and identified Ni/ZrO_2-SiO_2 to be a promising material based on high dynamic adsorption capacity, high VOC conversion, and turnover frequency. In a typical DFM, the VOC molecule first adsorbs onto the adsorbent active sites, then after desorption upon heating, it transfers to the adjacent catalytic sites where it is oxidized in the presence of O_2. In our previous contribution to numerical studies of adsorption of VOCs, (Adebayo et al., 2020b) we modeled adsorption of benzene in a TiO_2/SiO_2 and ZrO_2/SiO_2 fixed-bed column. The results revealed an accurate prediction of the capture process with a correct estimation of the KPIs.

In this investigation, we expanded the scope of our work on VOCs abatement and simulated a cyclic temperature swing adsorption-oxidation (TSAO) process that can concentrate VOC (benzene) during the adsorption step and then after desorption, oxidize it to water and carbon dioxide over Ni/ZrO_2-SiO_2. Our first objective was to formulate a robust mathematical model that describes the dynamics of the TSAO process, and then numerically simulate the model, while our second objective was to validate the model predictions against experimental adsorption and desorption/catalytic oxidation data. We also aimed at carrying out parametric analysis to assess the impacts of the process operating conditions on the KPIs.

2. Process description and modeling activities

2.1. Process description

The TSAO steps in this study are schematically shown in Fig. 1. The four sequential steps consist of adsorption, preheating, desorption/oxidation, and cooling. In the first step, a benzene-laden stream (c ppm$_v$ benzene in Ar) was fed into the bed at a specified flow rate, $v_{f,ads}$, and temperature, $T_{f,ads}$, for adsorption to take place in a bed initially equilibrated at adsorption temperature, T_{ads}, and pressure (1 atm). After the benzene concentration at the outlet reached 95% of its inlet concentration, the benzene-laden feed was replaced with a 10 mL/min air stream as the bed was preheated by a furnace to desorption temperature, T_{des}, at 25 K/min to initiate the desorption. The desorption temperature was estimated from our experimental work and its attainment marked the end of the preheating step (Adebayo et al., 2020c). It should be noted that the experimental runs were carefully carried out to ensure little or no desorption takes place during this step. In the next step (i.e., the desorption/oxidation step), the bed was heated from the desorption temperature to the oxidation temperature, T_{oxi}, while passing air to the bed to initiate the oxidation of benzene over the DFM. When the benzene concentration in the effluent stream reached zero, the desorption/oxidation step was assumed completed. It is important to mention that regeneration in this work comprises of preheating followed by desorption/oxidation. The inlet flow was then switched from air to Ar at a specified flow rate, $v_{f,cool}$, and the furnace opened to the lab conditions to cool the bed back to the adsorption temperature, T_{ads}. Prior to the beginning of the adsorption step, the bed was purged with 20 mL/min Ar flow for 2 h at T_{ads}, then allowed to get stabilized for 15 min. It is worth mentioning here that the gas streams during adsorption and desorption/oxidation steps were fed co-currently because the residence time during oxidation becomes greater as VOC will travel from the feed to the product end of the reactor.

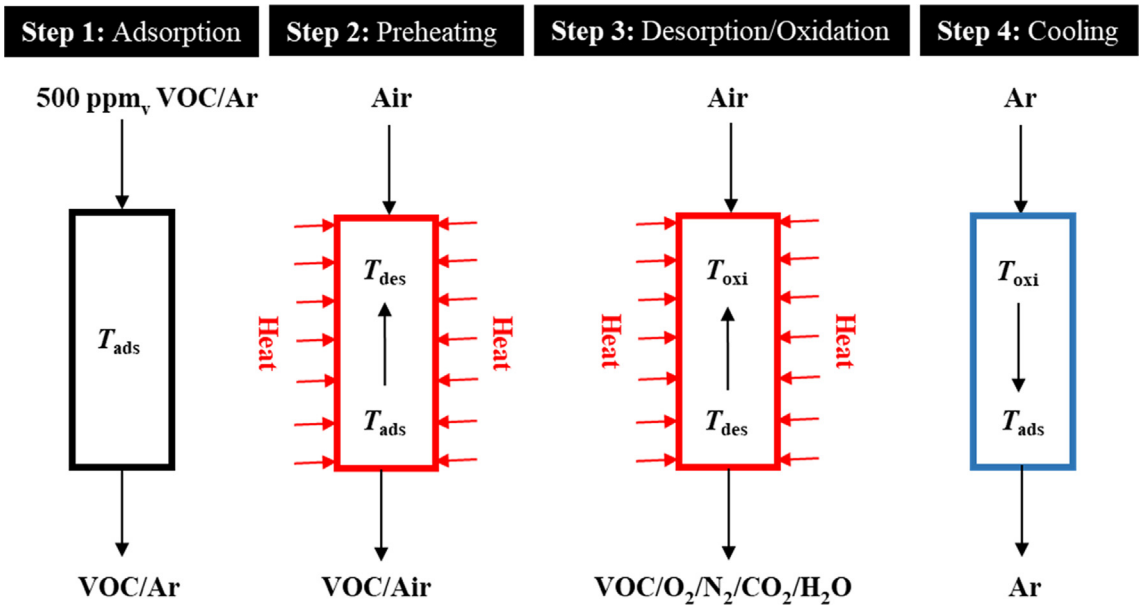

Fig. 1. Illustration of the four-step TSAO process investigated in this study.

In this manner, only a small amount of the desorbed VOC can exit the reactor due to its increased residence time for complete oxidation (Kolade et al., 2009). Throughout the TSAO laboratory runs, the bed outlet composition was monitored online using a mass spectrometer (MS BELMass), while the bed center temperature was recorded by an Omega Type-T thermocouple. The experimental setup has been fully described in our previous paper (Adebayo et al., 2020c). Also worth noting here that the feed gas (benzene in Ar) may not be representative of real industrial VOC-laden streams; similarly, cooling down a large-scale process with Ar may not be economically feasible; nonetheless, Ar was used in this study to facilitate the experiments especially with regards to tracking the CO production (as a by-product) during benzene oxidation which would have been difficult with N_2 as a career gas or cooling medium due to CO and N_2 same mass/charge ratio of 28.

2.2. Modeling activities

2.2.1. Model development

The model development consists of momentum, mass, and energy balance equations along with some auxiliary and constitutive correlations (as shown in the Supporting Information). The balance equations were developed to model the physiochemical processes that transpired during the TSAO process based on the principles of the laws of conservation for bulk gas and solid phases. The bulk gas phase was modeled as being one-dimensional along the bed axial direction, while the solid phase was modeled as being two-dimensional along the bed axial and the particle radial directions.

The model equations are written based on the following assumptions:

- DFM particles are spherical.
- System individual gases and their mixture are ideal.
- Physical, kinetic, and transport properties of the system are constant within individual steps but not necessarily constant among the steps.
- Local thermal equilibrium exists between the particle gas phase (the pore gas) and the solid phase.
- The benzene adsorption rate follows the linear driving force (LDF) model.
- The flow is described by an axial-dispersed plug model.
- The velocity, concentration, and temperature gradients along the radial direction are negligible for the bulk gas phase.

The mass balance for each of the components in the bulk gas phase was modeled by using Eq. (1): (Adebayo et al., 2020b)

$$\frac{\partial c_{b,i}(z)}{\partial t} = -\frac{\partial [u(z)c_{b,i}(z)]}{\partial z} + D_{ax,i}\frac{\partial^2 c_{b,i}(z)}{\partial z^2} + \frac{1-\varepsilon_b}{\varepsilon_b}A_{pa}k_{F,i}\left[c_{p,i}(z,r)\middle|r = r_{pa} - c_{b,i}(z)\right] \quad (1)$$

where i∈{VOC, Ar, O_2, N_2, CO_2, H_2O}.

Total mass balance was used to model the axial velocity variation along the bed, which is represented by Eq. (2):

$$\frac{\partial c_b(z)}{\partial t} = -\frac{\partial [u(z)c_b(z)]}{\partial z} + \frac{1-\varepsilon_b}{\varepsilon_b}A_{pa} \times \sum_{i=1}^{n_{cp}} k_{F,i}\left[c_{p,i}(z,r)\middle|r = r_{pa} - c_{b,i}(z)\right] \quad (2)$$

In the solid phase, the component mass balance was modeled by using Eq. (3): (Adebayo et al., 2020b)

$$\frac{\partial c_{p,i}(z,r)}{\partial t} = \frac{D_{eff,p,i}}{r^2}\frac{\partial}{\partial r}\left[r^2\frac{\partial c_{p,i}(z,r)}{\partial r}\right] - \rho_{pa}\left[\frac{1-\varepsilon_{pa}}{\varepsilon_{pa}}R_{sor}(z,r) + v_i R_{oxi}(z,r)\right] \quad (3)$$

The VOC sorption (adsorption or desorption) rate, R_{sor} [mol/kg/s] was modeled by using the LDF model, first propounded by Glueckauf and Coates: (Glueckauf and Coates, 1947)

$$R_{sor}(z,r) = k_{LDF}(z,r)\left[q_{eq}(z,r) - q(z,r)\right] \quad (4)$$

To cover the entire pressure domain attainable in all the steps, the benzene adsorption isotherms are fitted by the BET isotherm model:

$$q_{eq}(z,r)=\frac{q_m(z,r)\ c_{BET}(z,r)\left(\frac{p_{p,VOC}(z,r)}{P^{sat}_{p,VOC}(z,r)}\right)}{\left\{1-\left(\frac{p_{p,VOC}(z,r)}{P^{sat}_{p,VOC}(z,r)}\right)\right\}\left[1-\{1-c_{BET}(z,r)\}\left(\frac{p_{p,VOC}(z,r)}{P^{sat}_{p,VOC}(z,r)}\right)\right]} \quad (5)$$

where the parameters q_m, c_{BET} and $P^{sat}_{p,VOC}$ are all temperature-dependent parameters, as defined in equations (S2-5) in the Supporting Information.

It was assumed that the rate of oxidation of the desorbed VOC, R_{oxi} [mol/kg/s] follows the Downie (Mars-van Krevelen) model: (Barresi and Baldi, 1992; Gangwal et al., 1988)

$$R_{oxi}(z,r)=\frac{k_{VOC}(z,r)k_{O_2}(z,r)c_{p,VOC}(z,r)c_{p,O_2}(z,r)}{k_{O_2}(z,r)c_{p,O_2}(z,r)+(-Stoic_{O_2})k_{VOC}(z,r)c_{p,VOC}(z,r)} \quad (6)$$

The benzene oxidation kinetic data used in the simulation were obtained from the work of Barresi and Baldi (1992) and Gangwal et al. (1988)

For a Newtonian fluid, the momentum balance equation for a one-dimensional flow along the axial direction was approximated by using the modified Ergun Eq. (7): (Bird, 2002)

$$-\frac{\partial P_b(z)}{\partial z}=\frac{150\mu_{b,g}(1-\varepsilon_b)^2}{\varepsilon_b^3(2r_{pa})^2}u(z)+\frac{1.75\rho_{b,g}(1-\varepsilon_b)}{\varepsilon_b^3(2r_{pa})}|u(z)|u(z)-\rho_{b,g}g \quad (7)$$

The differential energy balance for the bulk gas phase was modeled by using Eq. (8):

$$\rho_{b,g}\hat{c}_{b,g,p}\frac{\partial T_b(z)}{\partial t}=-\rho_{b,g}\hat{c}_{p,g,p}\frac{\partial[u(z)T_b(z)]}{\partial z}+\lambda_{ax}\frac{\partial^2 T_b(z)}{\partial z^2}+\frac{1-\varepsilon_b}{\varepsilon_b}h_F A_{pa}[T_{pa}(z,r)|r=r_{pa}-T_b(z)]-\frac{A_b h_{int}}{\varepsilon_b}[T_b(z)-T_w(z)] \quad (8)$$

whereas Eq. (9) was used to describe the energy balance inside the particles:

$$\left[\varepsilon_{pa}\rho_{p,g}\hat{c}_{p,g,p}+(1-\varepsilon_{pa})\rho_s\hat{c}_s\right]\frac{\partial T_{pa}(z,r)}{\partial t}=\frac{\lambda_{eff}}{r^2}\frac{\partial}{\partial r}\left[r^2\frac{\partial T_{pa}(z,r)}{\partial r}\right]-\rho_{pa}[R_{sor}(z,r)\Delta H_{sor}(z,r)+R_{oxi}(z,r)\Delta H_{oxi}(z,r)] \quad (9)$$

The wall energy balance was accounted for by using Eq. (10): (Yang et al., 1997)

$$\hat{c}_c\rho_c\frac{\partial T_w(z)}{\partial t}=A_{int}h_{int}[T_b(z)-T_w(z)]-A_{ext}h_{ext}[T_w(z)-T_a] \quad (10)$$

The boundary conditions specific to the above model equations are presented in Table 1, while all other equations and correlations implemented in the code are presented in the Supporting Information. The initial conditions for the adsorption step in the first cycle are also presented in Table 1. The results obtained in each step of the process were used as the initial conditions for the next step.

2.2.2. Process simulation

The model equations described above were coded in **gPROMS**® ModelBuilder version 5.1.1, (Process Systems Enterprise, 1997–2020) and then solved by the method of lines (MOL), discretizing the bed axial and particle radial domains using the second-order backward finite difference method (BFDM) and the second-order orthogonal collocation on finite elements method (OCFEM), respectively, thus resulting in mixed sets of time-dependent ordinary differential and algebraic equations (DAEs). Thereafter, the time integration was performed by the DAE solver DASOLV, which thus reduced the DAEs to a set of algebraic simultaneous equations (AEs) per integration time. Finally, the resulting set of AEs was solved over time by BDNLSOL (Block Decomposition NonLinear SOLver). For all the simulation runs, absolute tolerance and relative tolerance values were set at 10^{-5} and 10^{-6} respectively. For the simulation to be node-independent, the number of nodes was increased until no further change was observed in the results. In this work, cyclic steady state (CSS) is defined as the state when the below equation is satisfied: (Effendy et al., 2017)

$$\Delta e_{i,j}\equiv e_{i,j}-e_{i,j+1}=\frac{1}{n_\chi}\sum_\chi\int_0^L\left|\chi_{i,j+1}-\chi_{i,j}\right|dz<\delta = 10^{-6}\times 100\% \quad (11)$$

where χ and n_χ represent the set of the performance variables and their number (here 3), i axial locations, and j cycle numbers.

The column design specifications used for all the modeling activities in this work are presented in Table 2.

2.2.3. Model validation

The prediction fidelity of the model was assessed by comparing the model predictions against the experimental data (**Run 1**) in Table 3. Additionally, **Run 2** was performed to specify model parameters such as axial diffusivities, and mass and heat transfer coefficients with the experimental data. It should be noted here that sensitivity analysis was not carried out in this investigation. For both runs, $T_0 = T_{a,0} = T_{b,0} = T_{f,0} = T_{w,0}$ and $c_0 = c_{b,0} = c_{p,0}$ with the concentration values constituting an ordered set of {VOC, Ar, O_2, N_2, CO_2, H_2O}. After a successful simulation of the TSAO model developed in the previous section, the model validation was executed in **gPROMS**® using its intrinsic maximum likelihood estimator (gEST) (Process Systems Enterprise, 1997–2020). For these activities, $y_{b,i}$ (L) = $c_{b,i}$ $(L)/c_b$ (L) and T_b $(0.5L)$ were used as the response variables. Moreover, it should be noted here that these activities were carried out only for the adsorption and the desorption/oxidation steps since they are the more important steps in the process. Besides, since the same model equations are used in all the steps other than the change in boundary conditions, it is expected that if the model works for adsorption and/or desorption/oxidation, then it definitely would work for every other step.

2.2.4. Parametric analysis

Designing cyclic adsorption processes involves many degrees of freedom which may be divided into two categories of parameters and factors. Examples of parameters are void fraction, density, heat capacity, and transport parameters. The factors which are the decision variables may be subdivided into design variables (column-related variables e.g., column dimension and heat transfer area) and operating conditions (operation-related variables e.g., feed conditions and step periods). In this work, our focus was primarily on the operating conditions and the investigation of their impact on the KPIs. The operating conditions considered in this work were adsorption feed conditions (VOC concentration, temperature, and flow rate), adsorption temperature, regeneration feed conditions (temperature and flow rate), and oxidation temperature, whereas the KPIs considered were adsorption efficiency, X_{ads} [%], oxidation efficiency, X_{des} [%], total removal efficiency, X_{rem} [%], and specific energy consumption, E_{spe} [J/mol]. In the absence of global system analysis (GSA) tool, a local system analysis (LSA) approach was considered in this work. LSA entails the variation of an operating condition per time while keeping others at their best-known values to ensure a systematic analysis. It should be noted that LSA does not take into consideration any interactions between operating conditions, though it is fast compared to GSA. The performance comparison was evaluated at CSS. The details of KPIs are as the following:

Table 1
Process model boundary and initial conditions.

$z = 0$	$z = L$
$u_f \sum_{i=1}^{n_{cp}} c_{f,i} = u(z)\ c_b(z)$	$\frac{\partial u(z)}{\partial z} = 0$
$-D_{ax,i} \frac{\partial c_{b,i}(z)}{\partial r} = u_f c_{f,i} - u(z)\ c_{b,i}(z)$	$\frac{\partial c_b(z)}{\partial z} = 0$
$-\lambda_{ax} \frac{\partial T_b(z)}{\partial z} = \rho_{b,g} \widehat{c}_{b,g,P}[u_f T_f - u(z) T_b(z)]$	$\frac{\partial T_b(z)}{\partial z} = 0$
	$\frac{\partial P_b(z)}{\partial z} = 0$
$0 \leqslant z \leqslant L,\ r = 0$	$0 \leqslant z \leqslant L,\ r = r_{pa}$
$\frac{\partial c_{p,i}(z,r)}{\partial r} = 0$	$-D_{eff,p,i} \frac{\partial c_{p,i}(z,r)}{\partial r} = k_{F,i}[c_{p,i}(z,r) - c_{b,i}(z)]$
$\frac{\partial T_{pa}(z,r)}{\partial r} = 0$	$-\lambda_{eff} \frac{\partial T_{pa}(z,r)}{\partial r} = h_F[T_{pa}(z,r) - T_b(z)]$
$t = 0$	
$c_{b,i}(z) = c_{b,0,i},\ \forall z \in (0, L)$	$T_b(z) = T_{b,0},\ \forall z \in (0, L)$
$c_b(z) = \sum_{i=1}^{n_{cp}} c_{b,0,i},\ \forall z \in (0, L)$	$T_{pa}(z,r) = T_{pa,0},\ \forall z \in (0, L),\ r \in [0, r_{pa}]$
$c_{p,i}(z,r) = c_{p,0,i},\ \forall z \in (0, L),\ r \in [0, r_{pa}]$	$T_w(z) = T_{w,0},\ \forall z \in [0, L]$
$q(z,r) = q_0,\ \forall z \in [0, L],\ r \in [0, r_{pa}]$	$T_a = T_{a,0}$
	$T_f = T_{f,0}$

Table 2
Particle, bed and column geometry and parameters used in simulations.

Parameter	Value	Parameter	Value
Geometry		*Parameters*	
d_{pa} [m]	3.55×10^{-6}	m [kg]	0.0002
L [m]	0.02	λ_c [W/m/K]	16.2
L_c [m]	0.1	$\hat{c}_c$ [J/kg/K]	500
d_{int} [m]	0.01	ρ_c [kg/m^3]	800
d_{ext} [m]	0.012	ρ_s [kg/m^3]	2200
v_{pa} [m^3/kg]	0.001	ΔH_{oxi} [J/mol]	−3300000

- Adsorption efficiency: It is the fraction of the feed gas that is captured during adsorption, which is a measure of the VOC adsorptive efficiency of the DFM and calculated by:

$$X_{ads} = \left(\frac{n_{f,VOC,ads} - n_{VOC,ads}\big|_{z=L}}{n_{f,VOC,ads}} \right) \times 100\% \tag{12}$$

where $n_{f,VOC,ads} = \int_0^{t_{ads}} c_{f,VOC,ads} u_{f,ads} dt$ is the molar amount of VOC fed to the bed during adsorption and $n_{VOC,ads}\big|_{z=L} = \int_0^{t_{ads}} c_{b,VOC,ads}\big|_{z=L} u_{ads}\big|_{z=L} dt$ the portion of which that exited the bed.

- Oxidation efficiency: It is the fraction of the desorbed VOC that is destructed via oxidation, which is a measure of the VOC catalytic destruction efficiency of the DFM and calculated by:

$$X_{oxi} = \left(\frac{\widetilde{\widetilde{n}}_{des} - n_{VOC,deo}\big|_{z=L}}{\widetilde{\widetilde{n}}_{des}} \right) \times 100\% \tag{13}$$

where $\widetilde{\widetilde{n}}_{des} = \frac{3m}{L r_{pa}^3} \int_0^L \left\{ \int_0^{r_{pa}} \left\{ r^2 \int_{t_{ads}}^{t_{ads}+t_{reg}} R_{des}(z,r) dt \right\} dr \right\} dz$ is the total amount of VOC desorbed during the desorption/oxidation step while $n_{VOC,deo}\big|_{z=L} = \int_{t_{pht}}^{t_{pht}+t_{deo}} c_{b,VOC,deo}\big|_{z=L} u_{deo}\big|_{z=L} dt$ [mol] is the portion of which that exited the bed.

- Removal efficiency: It is the fraction of the VOC in the feed gas that is removed during both adsorption and regeneration steps. It is a measure of the total removal efficiency of the hybrid VOC abatement process and is calculated by (Kolade et al., 2009; Miguel et al., 2017):

$$X_{rem} = \left(\frac{n_{f,VOC,ads} - n_{VOC,ads+reg}\big|_{z=L}}{n_{f,VOC,ads}} \right) \times 100\% \tag{14}$$

Table 3
TSAO experimental conditions for model validation and parameter estimation.

Run	Parameter	Value	Parameter	Value
1	$c_{f,ads}$ [mol/m^3]	[0.02, 40.86, 0, 0, 0, 0]	$\dot{v}_{f,deo}$ [mL/min]	20
	$c_{f,pht}$ [mol/m^3]	[0, 0, 8.58, 32.29, 0, 0]	$\dot{v}_{f,cool}$ [mL/min]	0
	$c_{f,deo}$ [mol/m^3]	[0, 0, 8.58, 32.29, 0, 0]	$T_{ads} = T_0$ [K]	308.15
	$c_{f,cool}$ [mol/m^3]	[0,0,0,0,0,0]	T_{des} [K]	373.15
	c_0 [mol/m^3]	[0, 40.88, 0, 0, 0, 0]	T_{oxi} [K]	473.15
	$T_{f,ads,0}$ [K]	298.15	t_{ads} [s]	5000
	$T_{f,pht,0}$ [K]	298.15	t_{pht} [s]	120
	$T_{f,cool,0}$ [K]	298.15	t_{deo} [s]	29,500
	$\dot{v}_{f,ads}$ [mL/min]	25	t_{cool} [s]	9315
	$\dot{v}_{f,pht}$ [mL/min]	20		
2 (Base Case)	$c_{f,ads}$ [mol/m^3]	[0.02, 40.86, 0, 0, 0, 0]	$\dot{v}_{f,deo}$ [mL/min]	10
	$c_{f,pht}$ [mol/m^3]	[0, 0, 8.58, 32.29, 0, 0]	$\dot{v}_{f,cool}$ [mL/min]	10
	$c_{f,deo}$ [mol/m^3]	[0, 0, 8.58, 32.29, 0, 0]	$T_{ads} = T_0$ [K]	298.15
	$c_{f,cool}$ [mol/m^3]	[0, 40.88, 0, 0, 0, 0]	T_{des} [K]	373.15
	c_0 [mol/m^3]	[0, 40.88, 0, 0, 0, 0]	T_{oxi} [K]	523.15
	$T_{f,ads,0}$ [K]	298.15	t_{ads} [s]	2550
	$T_{f,pht,0}$ [K]	298.15	t_{pht} [s]	120
	$T_{f,cool,0}$ [K]	298.15	t_{deo} [s]	26,570
	$\dot{v}_{f,ads}$ [mL/min]	100	t_{cool} [s]	6000
	$\dot{v}_{f,pht}$ [mL/min]	10		

where $n_{\mathrm{VOC,ads+reg}}\big|_{z=L} = n_{\mathrm{VOC,ads}}\big|_{z=L} + n_{\mathrm{VOC,reg}}\big|_{z=L}$ is the VOC molar amount that exited the bed during adsorption and regeneration.

- Specific energy consumption: It is the total energy consumed by the TSAO unit over a given cycle divided by the mole of VOC desorbed (Joss et al., 2017):

$$E_{\mathrm{spe}} = \frac{\int_0^{t_{\mathrm{cycle}}} \max(0, E_{\mathrm{eir}})dt}{\tilde{\tilde{n}}_{\mathrm{des}}} \tag{15}$$

where E_{eir} is calculated by using Eq. (16):

$$\text{During adsorption, } E_{\mathrm{eir}} = 0 \tag{16a}$$

$$\text{During preheating, } E_{\mathrm{eir}} = h_{\mathrm{r}}\left(m\hat{c}_{\mathrm{s}} + \tilde{m}_{\mathrm{b,g}}\hat{c}_{\mathrm{b,g,P}} + \tilde{\tilde{m}}_{\mathrm{p,g}}\hat{c}_{\mathrm{p,g,P}} + \tilde{\tilde{m}}_{\mathrm{ads}}\hat{c}_{\mathrm{adp}}\right)(T_{\mathrm{des}} - T_{\mathrm{ads}}) \tag{16b}$$

During desorption/oxidation,

$$E_{\mathrm{eir}} = h_{\mathrm{r}}\left(m\hat{c}_{\mathrm{s}} + \tilde{m}_{\mathrm{b,g}}\hat{c}_{\mathrm{b,g,P}} + \tilde{\tilde{m}}_{\mathrm{p,g}}\hat{c}_{\mathrm{p,g,P}} + \tilde{\tilde{m}}_{\mathrm{ads}}\hat{c}_{\mathrm{adp}}\right)(T_{\mathrm{oxi}} - T_{\mathrm{des}}) + \tilde{\tilde{n}}_{\mathrm{des}}\left[-\tilde{\tilde{\mathrm{K}}}_{\mathrm{ads}}\Delta\tilde{\tilde{H}}_{\mathrm{ads}} + \tilde{\tilde{\mathrm{K}}}_{\mathrm{rea}}\left(\tilde{\tilde{\mathrm{E}}}_{\mathrm{a}} - \Delta\tilde{\tilde{H}}_{\mathrm{rea}}\right)\right] \tag{16c}$$

$$\text{During cooling, } E_{\mathrm{eir}} = -h_{\mathrm{r}}\left(m\hat{c}_{\mathrm{s}} + \tilde{m}_{\mathrm{b,g}}\hat{c}_{\mathrm{b,g,P}} + \tilde{\tilde{m}}_{\mathrm{p,g}}\hat{c}_{\mathrm{p,g,P}}\right)(T_{\mathrm{oxi}} - T_{\mathrm{cool}}) \tag{16d}$$

where $\tilde{\tilde{m}}_{\mathrm{ads}} = \tilde{\tilde{n}}_{\mathrm{ads}} \times M_{\mathrm{VOC}}$ and $\hat{c}_{\mathrm{adp}} \cong \hat{c}_{\mathrm{g,P}}$. Throughout this work, the first three KPIs may be jointly called *efficiency KPIs*. It should be noted that in small reactors, walls have a very significant capacitive contribution and thus the effects have been eliminated from energy consumption Eq. (16a-d).

3. Results and discussion

3.1. Benzene adsorption isotherm fitting

The equilibrium adsorption isotherms of benzene at three different temperatures (25, 40, and 55 °C) were collected on a volumetric gas analyzer (3Flex, Micromeritics) and fitted with the BET isotherm model, as shown in Fig. 2. The adsorption uptake decreased with temperature across the entire pressure domain. The BET isotherm model was fitted to the experimental isotherm data using a multivariable, nonlinear least-squares method by minimizing the sum of the squared residuals between the model predictions and the experimental data. The fittings demonstrated excellent agreement (ca. $R^2 > 0.99$) between the model and experimental data across the entire pressure range, and at all temperatures. The estimated values of the BET temperature-independent parameters α_1 and α_2 described in equation (S10) in the Supporting Information were found to be 0.75 mol/kg and −8.51, respectively.

3.2. Model validation

The comparisons between the model predictions of the response variables and the experimental results are provided in Figs. 3–4 for **Run 1** and Fig. S1-S2 (Supporting Information) for **Run 2.** A relatively good agreement between the model predictions and the experimental observations was obtained for both runs. The estimated values of the model parameters for both adsorption and desorption/oxidation steps, together with their 95% confidence intervals (CIs) are shown in Table 4. The narrow CIs for all the parameters indicate that the precision in their estimation is statistically satisfactory. Both $y_{\mathrm{b,VOC}}(L)$ (Fig. S1a) and $T_{\mathrm{b}}(0.5L)$ (Fig. S1b)

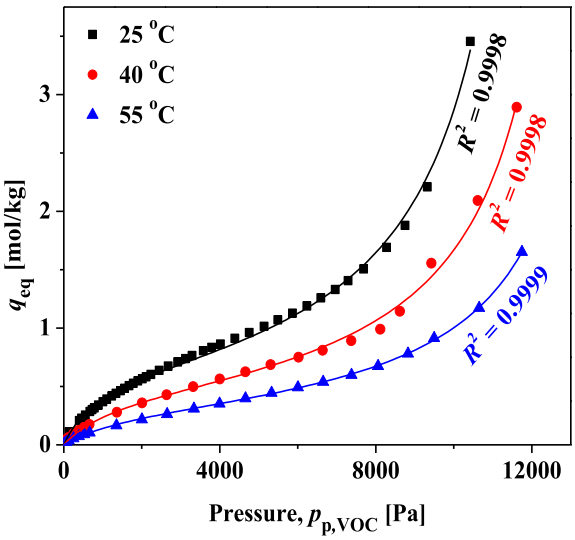

Fig. 2. Adsorption isotherms of benzene over Ni/ZrO_2-SiO_2 at different temperatures; symbols: experimental data; solid lines: data curve fittings with BET isotherm model.

were predicted with good accuracy. It should be noted here that the choice of the model assumptions was based on the diameter/length ratio of the column and the particle-to-column diameter ratio within the adsorber, however due to small size of the experimental setup, the reproducibility of the results at a larger scale may not be achieved.

3.3. TSAO base-case simulations

To facilitate the benchmarking, simulations were carried out for a "base-case" scenario of the TSAO process (i.e., **Run 2**). Fig. 5a-c shows the bed-exit bulk gas benzene mole fraction and particle surface adsorbed benzene concentration, and bed-center bulk gas temperature profiles obtained at the first cycle. In Fig. 5a, **5**% breakthrough and saturation occurred at ~1000 and 2550 s, respectively. As shown in Fig. 5b, adsorbed VOC concentration attained a maximum of 0.13 mol/kg compared to the 0.14 mol/kg equilibrium value at 25 °C (Fig. 2), followed by a very fast desorption. Fig. S3 in the Supporting Information reveals that the sorbent loading was not reduced during the preheating step: it started reducing only after the desorption temperature was attained. The sensible heat supplied during this step was to increase the temperature of the bed to the desorption temperature, while the latent heat provided the heat required to break the forces of attraction between the adsorbate and the DFM. The ramping of the bed from adsorption temperature to oxidation temperature passing through the desorption temperature was very fast, as can be seen in Fig. 5c. Similarly, the temperature increase during oxidation was successfully captured by the model, as evident in Fig. 5c. At the final step (i.e., the cooling step), bed temperature decreased rapidly to near 25 °C, whereby setting the TSAO process ready for another cycle.

The profiles of the base-case simulations up to CSS are depicted in Fig. 6. As described in Section 2.2.2, Eq. (11) was satisfied upon attaining the 3rd cycle with a relative tolerance value of 10^{-6} between cycles 2 and 3, indicating that CSS condition was reached. Fig. 6d shows the variation of outlet concentration over multiple TSAO cycles. Typically, CSS is obtained quickly during TSA, (Rezaei et al., 2014; Bonjour et al., 2002; Ko et al., 2001) and this constitutes an advantage of TSA over PSA, where a large number of cycles is usually required to attain CSS and subsequently improves performance (Shokroo et al., 2014). With the set of oper-

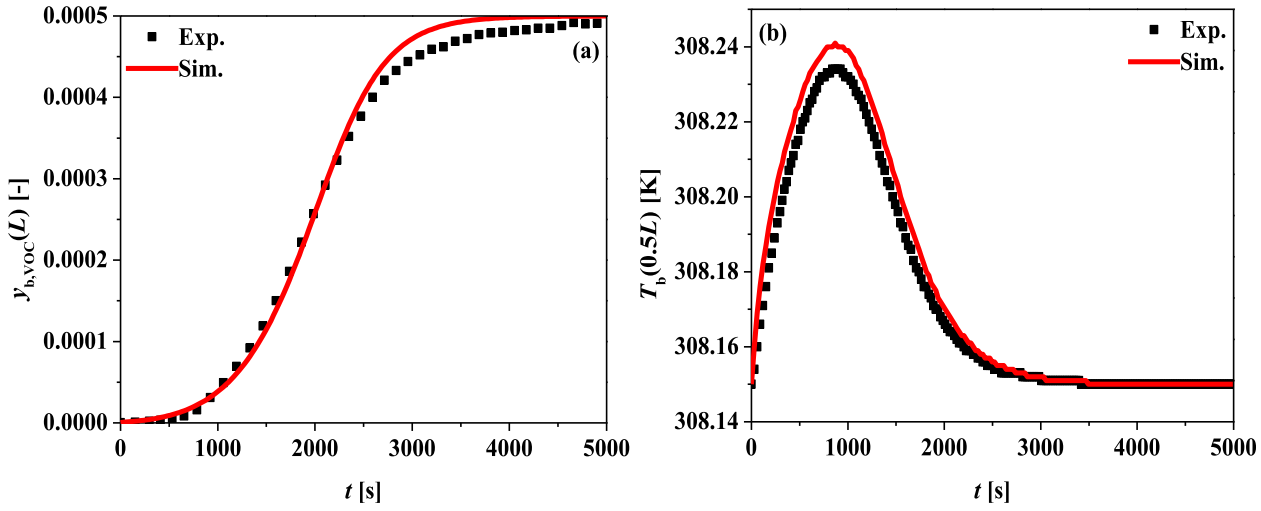

Fig. 3. Adsorption step fitting for model validation purpose, Run 1: (a) bed-exit bulk gas VOC molar fraction and (b) bed-center bulk gas temperature. Bed initial condition: Ar-saturated at 25 °C and 1 atm; adsorptive feed: 500 ppm_v VOC, 25 °C, 1 atm and 100 mL/min.

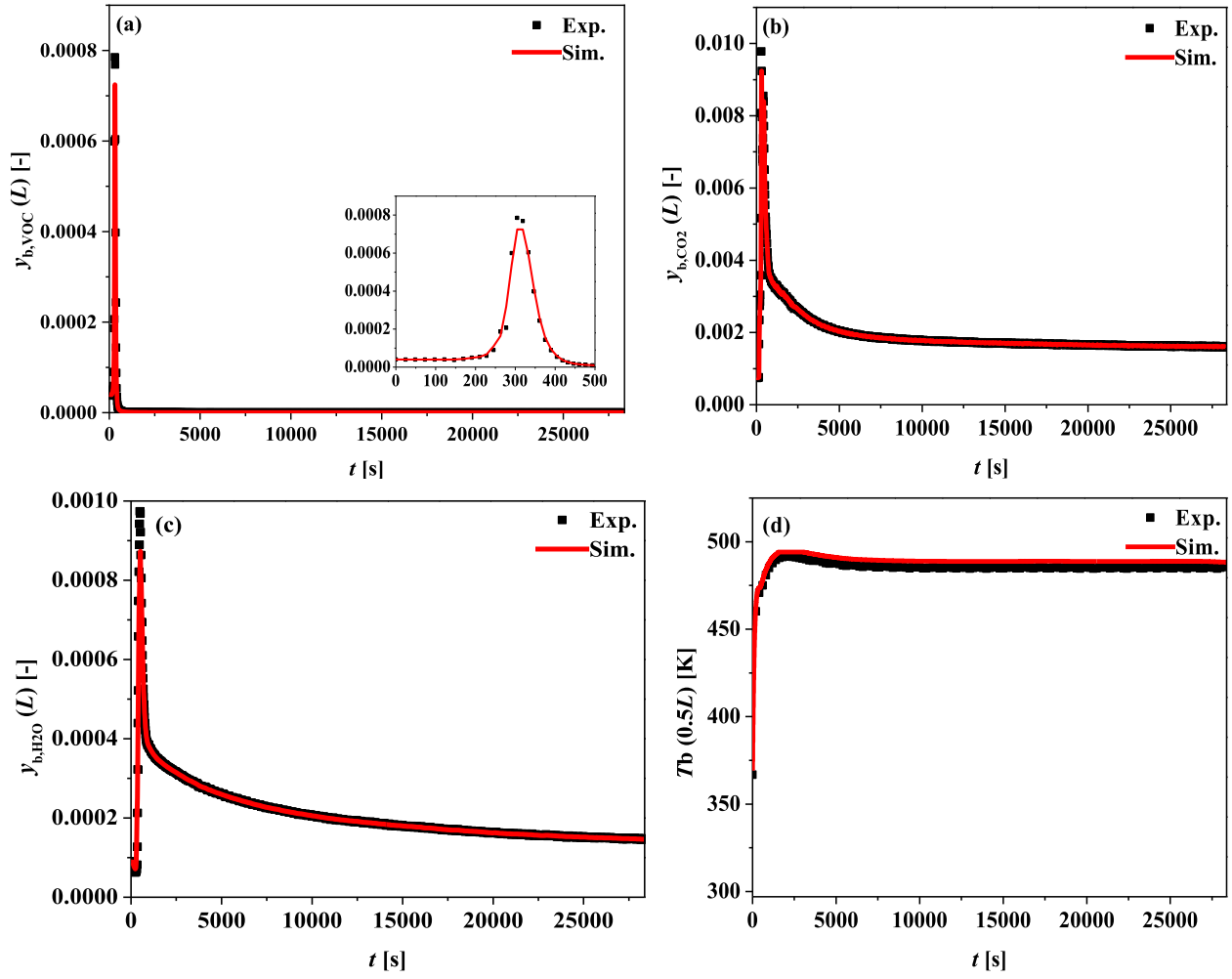

Fig. 4. Desorption/oxidation step fitting for model validation purpose, Run 1: bed-exit bulk gas VOC molar fraction for (a) VOC, (b) CO_2, (c) H_2O, and (d) bed-center bulk gas temperature. The inset shows Fig. 4**a** in the first 500 s. Bed initial condition: Ar-saturated at 25 °C and 1 atm; adsorptive feed: 500 ppm_v VOC, 25 °C, 1 atm and 100 mL/min.

Table 4
Estimated values of the model parameters with their 95% CIs.

Parameter	Value	95% CI	Parameter	Value	95% CI
Adsorption					
$D_{ax,VOC}$ [m^2/s]	9.99×10^{-6}	6.52×10^{-8}	$k_{f,VOC}$ [m/s]	1.23×10^{-3}	2.69×10^{-7}
$D_{ax,Ar}$ [m^2/s]	1.30×10^{-11}	5.94×10^{-12}	$k_{f,Ar}$ [m/s]	3.51×10^{-6}	8.41×10^{-8}
h_f [$W/m^2/K$]	19.6	0.08388			
Desorption/Oxidation					
$D_{ax,VOC}$ [m^2/s]	4.93×10^{-6}	3.57×10^{-7}	$k_{f,VOC}$ [m/s]	0.027	1.09×10^{-7}
D_{ax,CO_2} [m^2/s]	8.13×10^{-6}	1.25×10^{-8}	k_{f,CO_2} [m/s]	0.039	7.16×10^{-7}
D_{ax,H_2O} [m^2/s]	1.10×10^{-5}	6.85×10^{-7}	k_{f,H_2O} [m/s]	0.049	2.35×10^{-7}
h_f [$W/m^2/K$]	107.36	0.057			

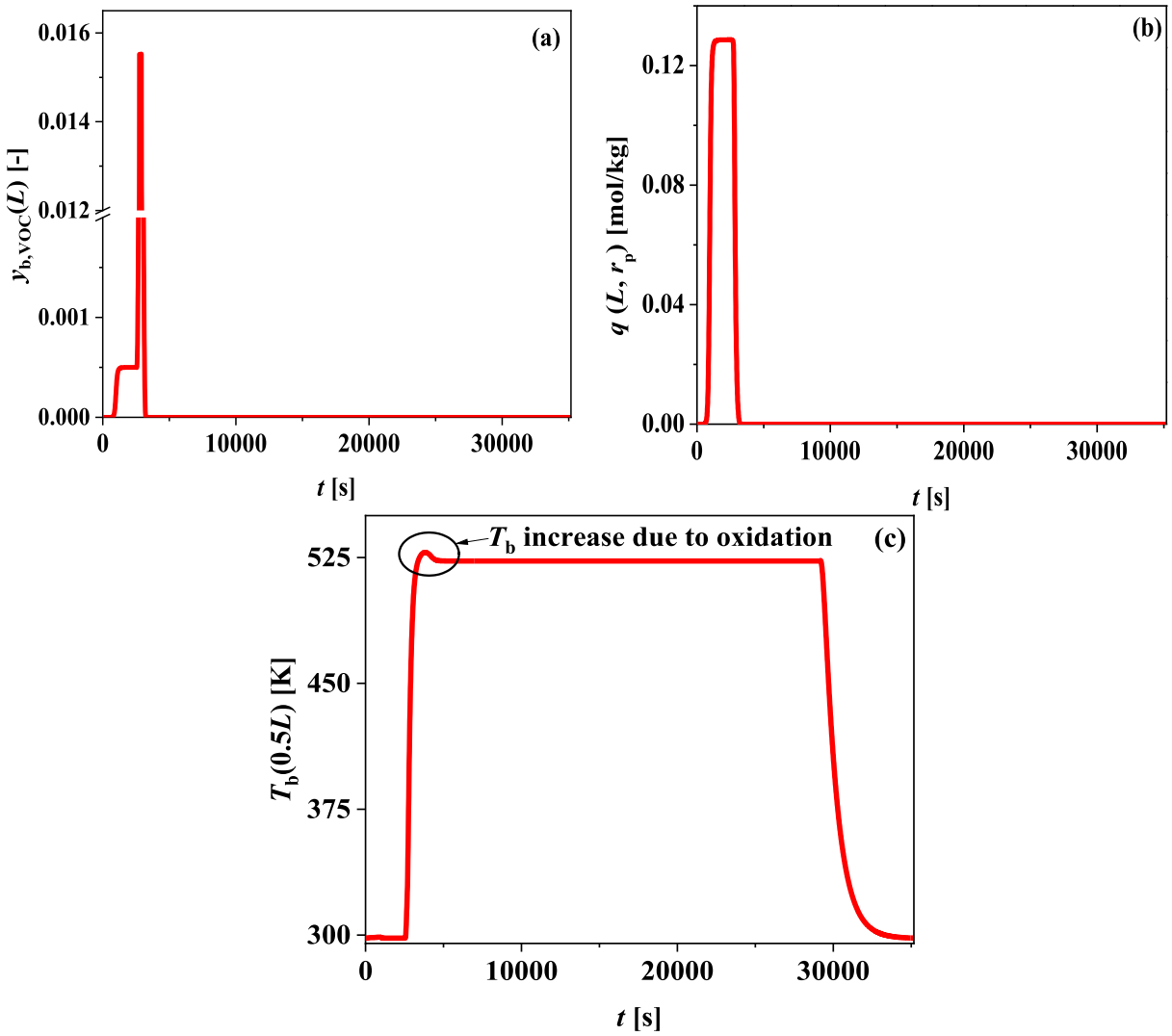

Fig. 5. TSAO base-case first cycle simulated profiles: (a) bed-exit bulk gas benzene concentration, (b) bed-exit particle surface adsorbed benzene concentration, and (c) bed-center bulk gas temperature. Bed initial condition: Ar-saturated at 25 °C and 1 atm; adsorptive feed: 500 ppm_v VOC, 25 °C, 1 atm and 100 mL/min; regenerative feed: 21%/79% O_2/N_2, 25 °C initial temperature, 1 atm and 10 mL/min; and cooling feed: pure Ar at 25 °C, 1 atm and 10 mL/min.

ating conditions used for the base-case simulations, an adsorption efficiency of 30%, oxidation efficiency of 49%, removal efficiency of 15%, and specific energy consumption of 316 MJ/mol were achieved at CSS. The corresponding values calculated from the experimental results were found to be 31%, 49.8%, 15%, and 320 MJ/mol. It should be mentioned that these values are unoptimized values and that the specific energy consumption is large mainly due to the long reaction period, about 7 h coupled with the high reaction temperature (523.15 K).

To test the predictive accuracy of the model for a TSAO cycle, the results of the TSAO base-case simulations at the first cycle were fitted against the corresponding experimental results, as shown in Fig. 7. As can be seen, all the process components bed-exit mole fraction profiles (Fig. 7a-f) were accurately predicted by the model, with an $R^2 > 0.95$. Likewise, the bulk temperature at the center of

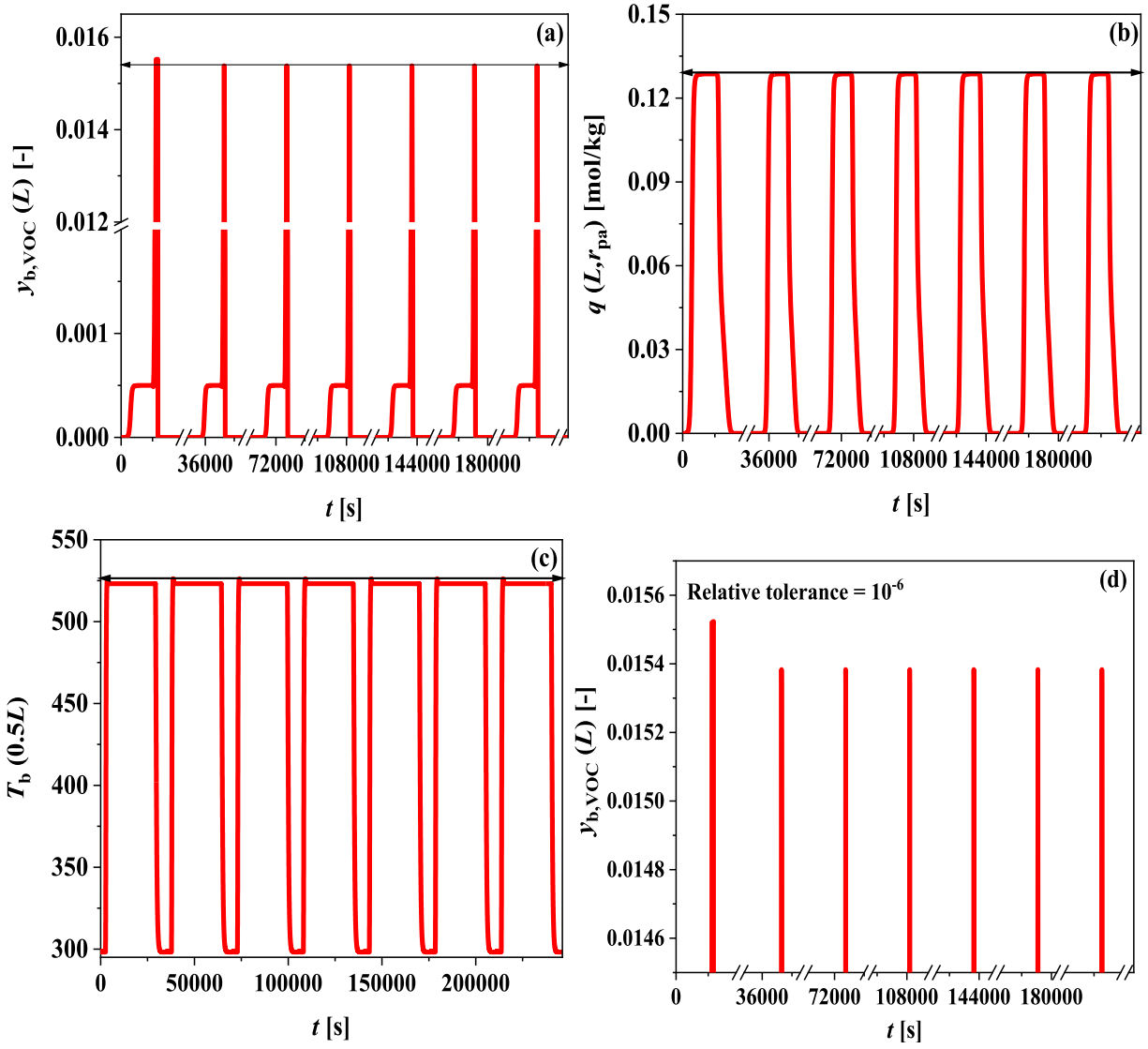

Fig. 6. TSAO base-case CSS simulated profiles: (a) bed-exit bulk gas benzene concentration, (b) bed-exit particle surface adsorbed benzene concentration, (c) bed-center bulk gas temperature, and (d) adjusted Fig. 6**a** showing the attainment of CSS. Bed initial condition: Ar-saturated at 25 °C and 1 atm; adsorptive feed: 500 ppm_v VOC, 25 °C, 1 atm and 100 mL/min; regenerative feed: 21%/79% O_2/N_2, 25 °C initial temperature, 1 atm and 10 mL/min; and cooling feed: pure Ar at 25 °C, 1 atm and 10 mL/min.

the bed was also satisfactorily predicted. All the expected trends and features were accurately captured. The point that marks the end of the desorption/oxidation step can be seen as being accurately predicted by the model as shown in Fig. 7e, f. Hence, it is conclusive that the model can be used to predict the TSAO process.

3.4. TSAO parametric analysis

3.4.1. Effects of adsorption feed conditions (VOC concentration, temperature, and flow rate)

The parametric analysis efforts were started with characterizing the effects of feed conditions on the defined KPIs. We first varied VOC concentration in the feed (5–1000 ppm_v) while keeping other operating conditions as in the base case. As shown in Fig. 8a, all the KPIs decreased with the feed VOC concentration. When the feed VOC concentration increased, bed saturation became faster (due to increased adsorption rate) resulting in higher bed saturation level and thus more VOC exiting the bed (Fig. S4 in Supporting Information). As more VOC exited the bed, both adsorption and removal efficiencies decreased as observed here. The loss in adsorption and removal efficiencies was expected since VOC feed concentration was increased at a fixed adsorption step time. At high bed saturation levels, oxidation efficiency decreased due to the high tendency for thermal runaway of the desorbed VOC as observed previousely (Urbutis and Kitrys, 2014). Increasing the feed VOC concentration increased the amount adsorbed and thereby the energy demand for regeneration (Delage et al., 2000). Under identical conditions, the amount desorbed increased with the amount adsorbed, hence the specific energy consumption decreased. Considering Eq. (15), it may not be quite straightforward to infer such finding as both energy demand for regeneration and amount desorbed increase simultaneously upon increasing feed concentration, however, this can be realized by considering the fact that at a given temperature the relative contribution of the sensible heat of the bed is equal in both cases mainly because the energy contribution related to the adsorber walls was excluded from the energy indicator. As shown in Fig. 8a, a reasonably low value of the specific energy consumption that keeps the efficiency KPIs as high as possible was found to be 50 ppm_v. At this specific concentration, the estimated values for adsorption, oxidation and removal efficiencies, and the specific energy consumption were 76.4, 74.6, 59.5%, and 316 MJ/mol respectively. Presented in

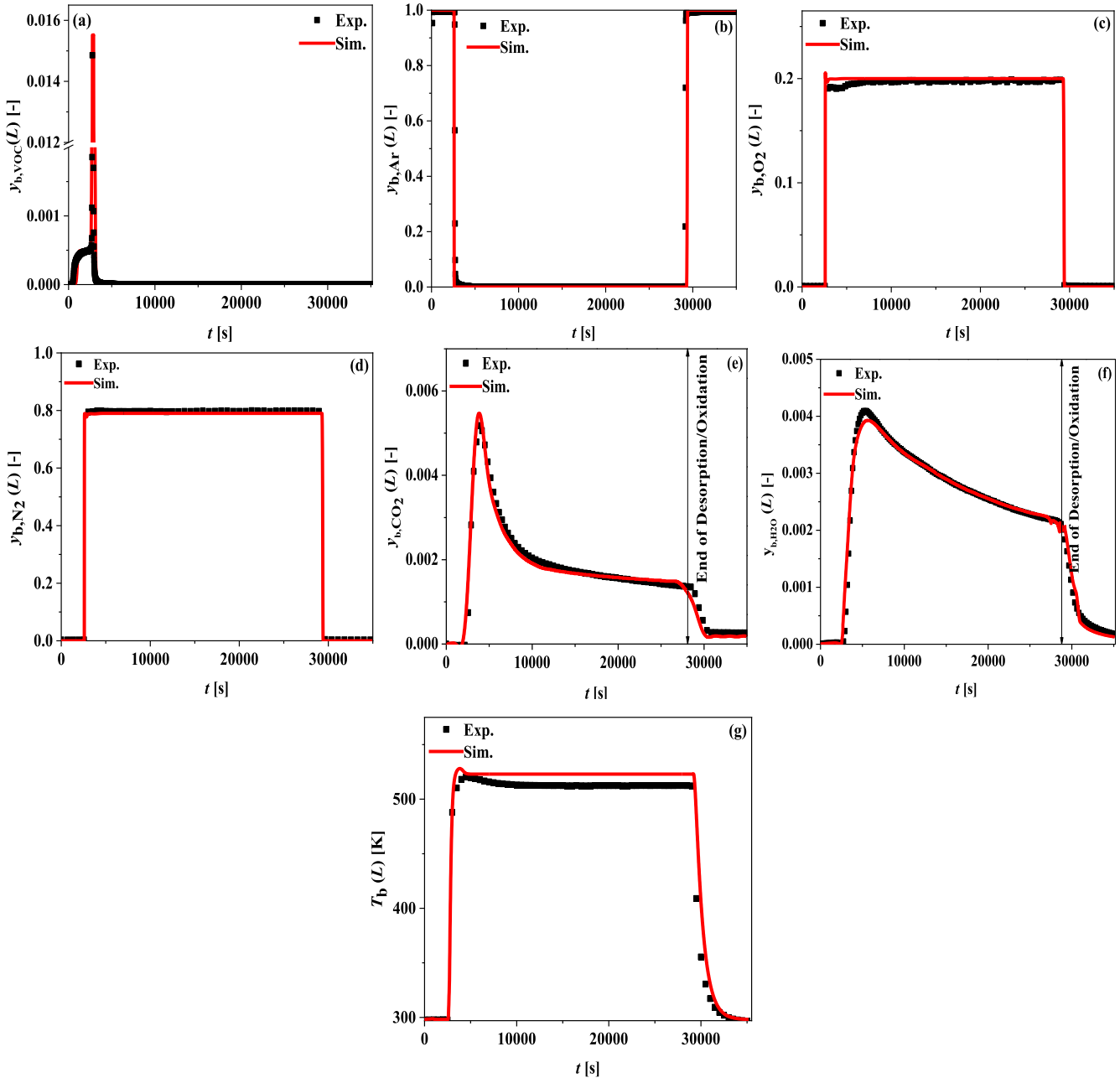

Fig. 7. Fittings of a complete cycle of the TSAO process with the corresponding experimental results: (a) VOC, (b) Ar, (c) O_2, (d) N_2, (e) CO_2, (f) H_2O mole fraction, and (g) temperature profiles. Bed initial condition: Ar-saturated at 25 °C and 1 atm; adsorptive feed: 500 ppm_v VOC, 25 °C, 1 atm and 100 mL/min; regenerative feed: 21%/79% O_2/N_2, 25 °C initial temperature, 1 atm and 10 mL/min; and cooling feed: pure Ar at 25 °C, 1 atm and 10 mL/min.

Fig. 8b are the effects of the adsorption feed temperature on the KPIs. Increasing the temperature increased the average kinetic energy of the VOC gas-phase molecules, thereby reducing the amount of VOC adsorbed. When the amount adsorbed decreased at a fixed adsorption period, the adsorption and the removal efficiencies reduced, while the oxidation efficiency and the specific energy consumption increased. Although the enhancement in the specific energy consumption with temperature is a non-straightforward effect among those observed, but it can be explained by the fact that high feed temperature decreased the amount of VOC adsorbed, which resulted in the loss in the amount of VOC desorbed, which in turn increased the specific energy consumption. Increasing the adsorption temperature, given the exothermic nature of adsorption, clearly is expected to be detrimental to the process performance, however, there might be potential advantages in terms of energy consumption, since the magnitude of the required temperature swing between adsorption and subsequent desorption/oxidation steps can be reduced accordingly. To keep the specific energy consumption low while maintaining high values of the efficiency KPIs, the feed temperature was set at 25 °C with KPI values of 76.4%, 74.6%, 59.5%, and 316 MJ/-mol for adsorption, oxidation and removal efficiencies, and specific energy consumption, respectively. Fig. 8c depicts the effects of feed flow rate (50–150 mL/min) on the KPIs. While the adsorption and the removal efficiencies decreased gradually with the flow rate, the specific energy consumption decreased abruptly till 100 mL/min and remained fairly constant thereafter, and the oxidation efficiency increased gradually. The decrease observed in the adsorp-

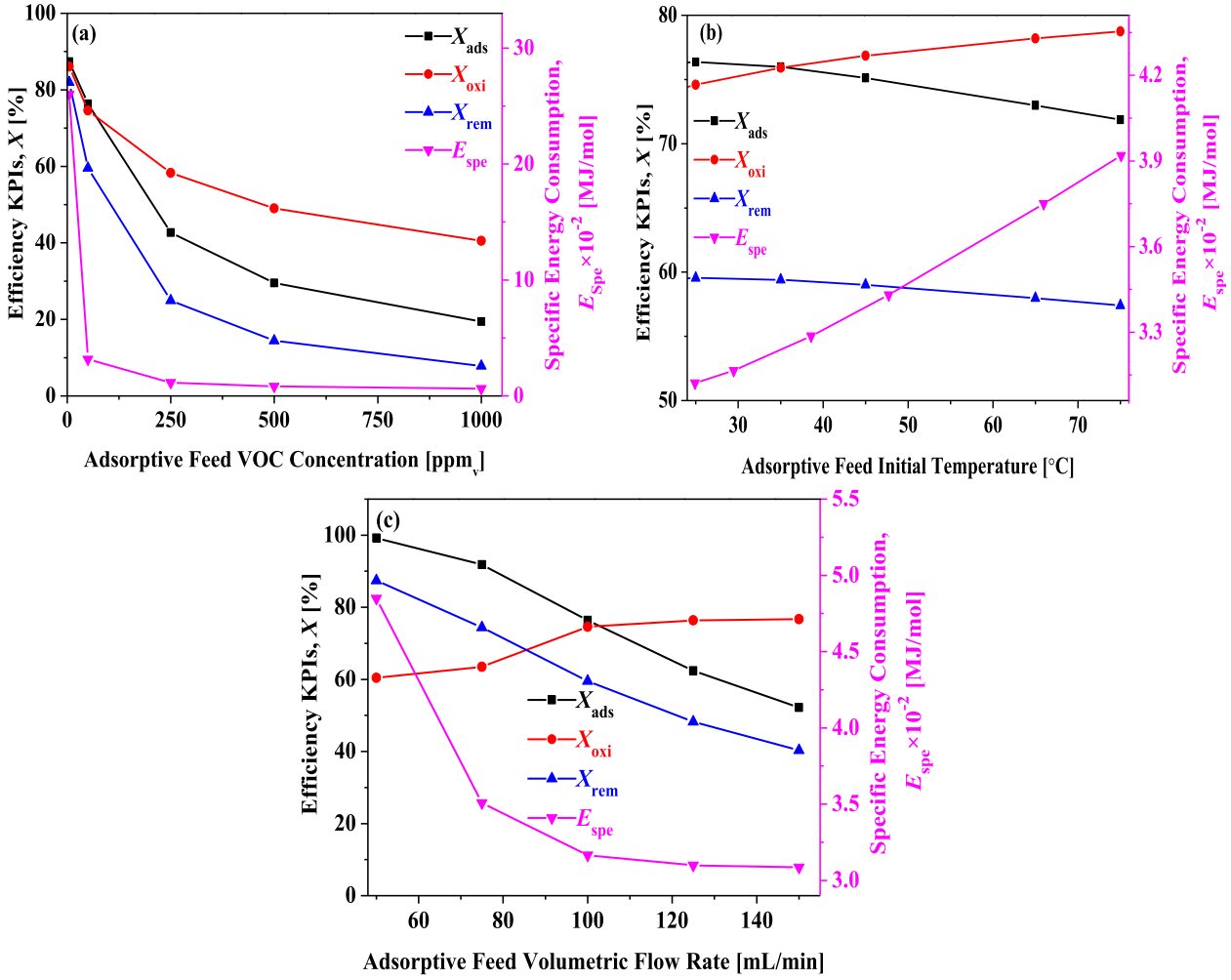

Fig. 8. Effects of (a) feed concentration ($c_{f,ads}$), (b) initial temperature ($T_{f,ads,0}$), and (c) flow rate ($\dot{v}_{f,ads}$) on the KPIs. Bed initial condition: Ar-saturated at 25 °C and 1 atm; adsorptive feed: 5–1000 ppm$_v$ VOC, 20–75 °C, 1 atm and 50–150 mL/min; regenerative feed: 21%/79% O_2/N_2, 25 °C initial temperature, 1 atm and 10 mL/min; and cooling feed: pure Ar at 25 °C, 1 atm and 10 mL/min.

tion and the removal efficiencies has been attributed to a lack of sufficient residence time during adsorption, i.e., faster breakthrough, (Ntiamoah et al., 2015) while the increase observed in the other two KPIs has been attributed to a lower bed saturation and consequent upon low thermal runaway. (Mitsuma et al., 1998) At 100 mL/min flow rate, the adsorption, oxidation and removal efficiencies were estimated to be 76.4, 74.6, and 59.5%, respectively, while the specific energy consumption was found to be 316 MJ/mol.

3.4.2. Effects of regeneration feed conditions (initial temperature and flow rate)

Here, the effects of the regeneration feed temperature (25–65 °C) and flow rate (5–100 mL/min) on the KPIs were investigated. In Fig. 9a, the adsorption efficiency remained constant, the oxidation and the removal efficiencies decreased linearly, while the specific energy consumption only slightly decreased with the temperature. The linear drop in these efficiencies with the regeneration temperature stems from the fact that at a fixed desorption/oxidation step time, the rate of desorption increases linearly, causing an increase in the amount of untreated VOC that exits the bed. Since the oxidation and the removal efficiencies were greatly reduced while their energy counterparts only slightly reduced as the regenerative feed temperature increased, it is conclusive that the regeneration feed temperature should be set as low as possible. Hence, setting the regenerative initial temperature at 25 °C resulted in adsorption, oxidation, and removal efficiencies and specific energy consumption of 76.4%, 74.6%, 59.5%, and 316 MJ/mol, respectively. In the case of regeneration feed flow rate, similar patterns were observed (see Fig. 9b). However, the decrease in the oxidation and the removal efficiencies in this case can be attributed to a shorter residence time of the regenerative O_2 within the DFM particles as substantiated by Urbutis and Kitrys (Urbutis and Kitrys, 2014). Similarly, this trend could also be due to the lower VOC thermal runaway at lower regenerative flow rate. The decrease in the specific energy consumption could be due to increase in the amount desorbed with increasing regenerative flow rate at constant energy consumption. At 5 mL/min flow rate, the adsorption, oxidation and removal efficiencies as well as the specific energy consumption were estimated to be 76.4%, 82.8%, 64.9%, and 312 MJ/mol, respectively.

3.4.3. Effects of adsorption, desorption, and oxidation temperatures

In the next step, adsorption, desorption and oxidation temperatures were varied in the range of 25–65 °C, 50–250 °C, and 170–270 °C, respectively, and the corresponding KPI values estimated in these temperature ranges are displayed in Fig. 10. In Fig. 10a, the adsorption and the removal efficiencies decreased with the adsorption temperature, whereas the oxidation efficiency increased slightly, and the specific energy consumption linearly.

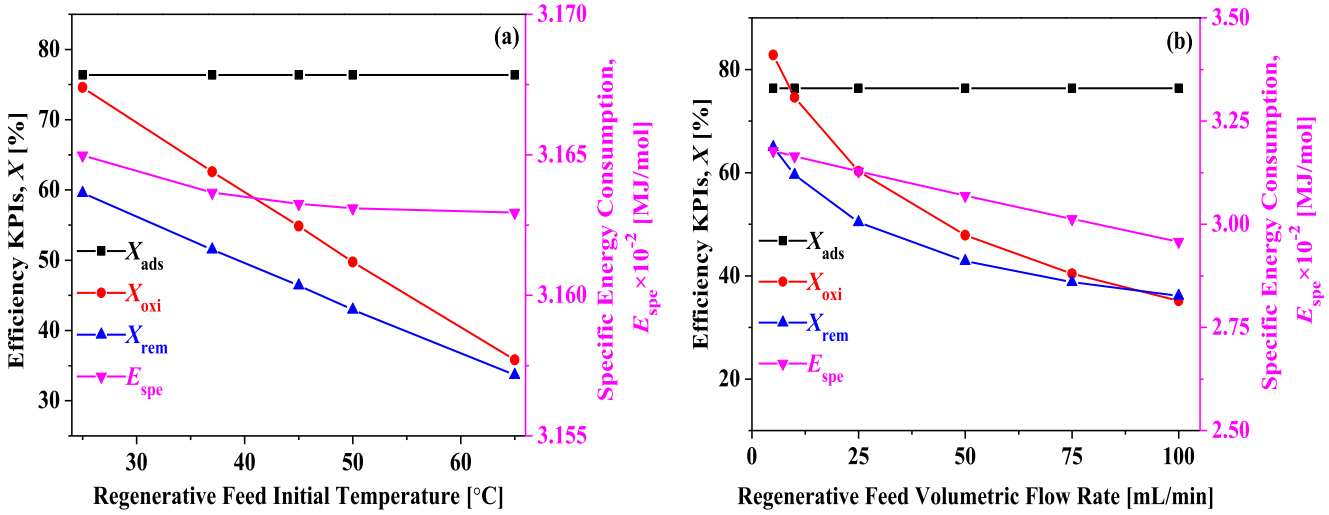

Fig. 9. Effects of (a) regeneration feed initial temperature ($T_{f,pht,0}$) and (b) flow rate ($\dot{v}_{f,pht} = \dot{v}_{f,deo}$) on the KPIs. Bed initial condition: Ar-saturated at 25 °C and 1 atm; bed initial conditions: adsorptive feed: 50 ppm_v VOC, 25 °C, 1 atm and 100 mL/min; regenerative feed: 21%/79% O_2/N_2, 25–65 °C initial temperature, 1 atm and 5–100 mL/min; and cooling feed: pure Ar at 25 °C, 1 atm and 10 mL/min.

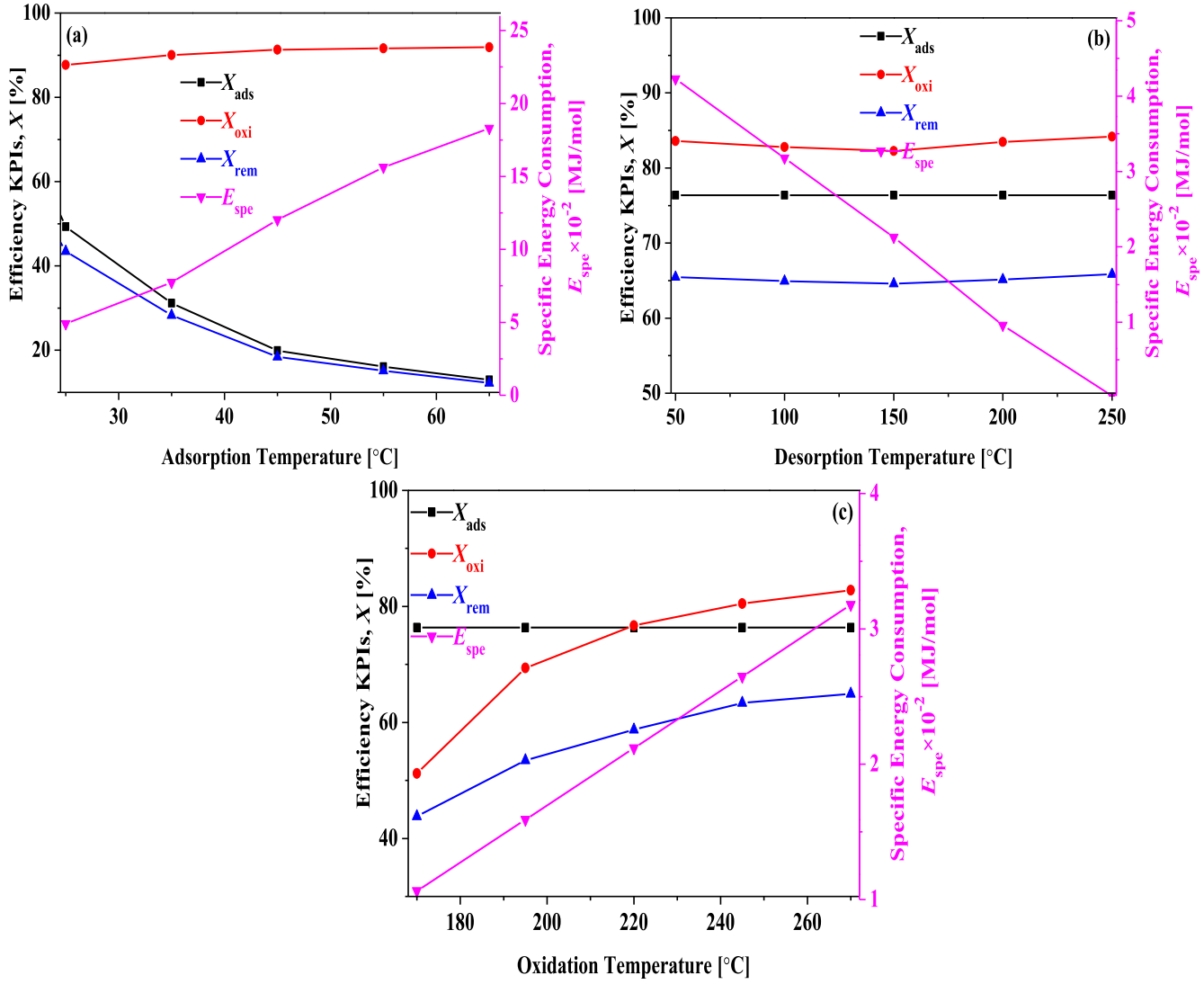

Fig. 10. Effects of (a) adsorption temperature (T_{ads}), (b) desorption temperature (T_{des}), and (c) oxidation temperature (T_{oxi}) on the KPIs. Bed initial condition: Ar-saturated at 25 °C and 1 atm; adsorptive feed: 50 ppm_v VOC, 25 °C, 1 atm and 100 mL/min; regenerative feed: 21%/79% O_2/N_2, 25 °C initial temperature, 1 atm and 5 mL/min; and cooling feed: pure Ar at 25 °C, 1 atm and 10 mL/min.

This is mainly because, at high adsorption temperatures, the bed is less saturated, thereby making desorbed VOC a limiting reactant to react with available excess O_2 (Huang et al., 2009). Increasing the adsorption temperature decreases the amount desorbed, and invariably the amount desorbed, thereby increasing the specific energy consumption. These results suggested that the adsorption temperature should be as low as possible for this hybrid TSAO process. At the adsorption temperature of 25 °C, the corresponding values of the adsorption, oxidation and removal efficiencies, and the specific energy consumption were estimated to be 76.4%, 82.8%, 64.9% and 318 MJ/mol, respectively. The variation in the KPI values as a function of desorption temperature is shown in Fig. 10b. Clearly, all the efficiency KPIs remained fairly unchanged (76.4, 83.9 and 65.6%, respectively for adsorption, oxidation and removal efficiencies), while the specific energy consumption dropped linearly from 96.1 to 23.9 MJ/mol when the desorption temperature was reduced from 250 to 50 °C. At a fixed set of operating conditions, the relative amount desorbed increased with the desorption temperature, hence the specific energy consumption decreased. This suggests that the desorption temperature should be close to the oxidation temperature as much as possible. Considering the effect of oxidation temperature (Fig. 10c), as expected, the adsorption efficiency was not affected (constant at 76.4%) by the oxidation temperature, primarily because in the Eq. (12) only adsorption terms were considered. Nevertheless, it should be noted here that in a cyclic process every single step has an influence on the operation of the whole cycle. On the contrary, the oxidation and the removal efficiencies and the specific energy consumption all increased with the oxidation temperature. (Campesi et al., 2012) Due to the clear trade-off between the efficiency KPIs and the specific energy consumption, the intersection of the removal efficiency and the specific energy consumption emerged as a suitable oxidation temperature: 230 °C. At this point, the adsorption, oxidation and removal efficiencies and the specific energy consumption were, respectively, 76.4%, 78.2%, and 60.6%, and 23.3 MJ/mol.

3.4.4. Effects of adsorption, preheating, desorption/oxidation and cooling periods

To assess the impact of step time on the performance of our hybrid TSAO process, the KPIs were estimated at different time periods and the results are presented in Fig. 11. The effects of the adsorption period were investigated between 750 and 4500 s, and as evident from Fig. 11a, while the adsorption and the removal efficiencies decreased linearly with the adsorption period, the oxidation efficiency slightly increased from 64.7% to attain a plateau

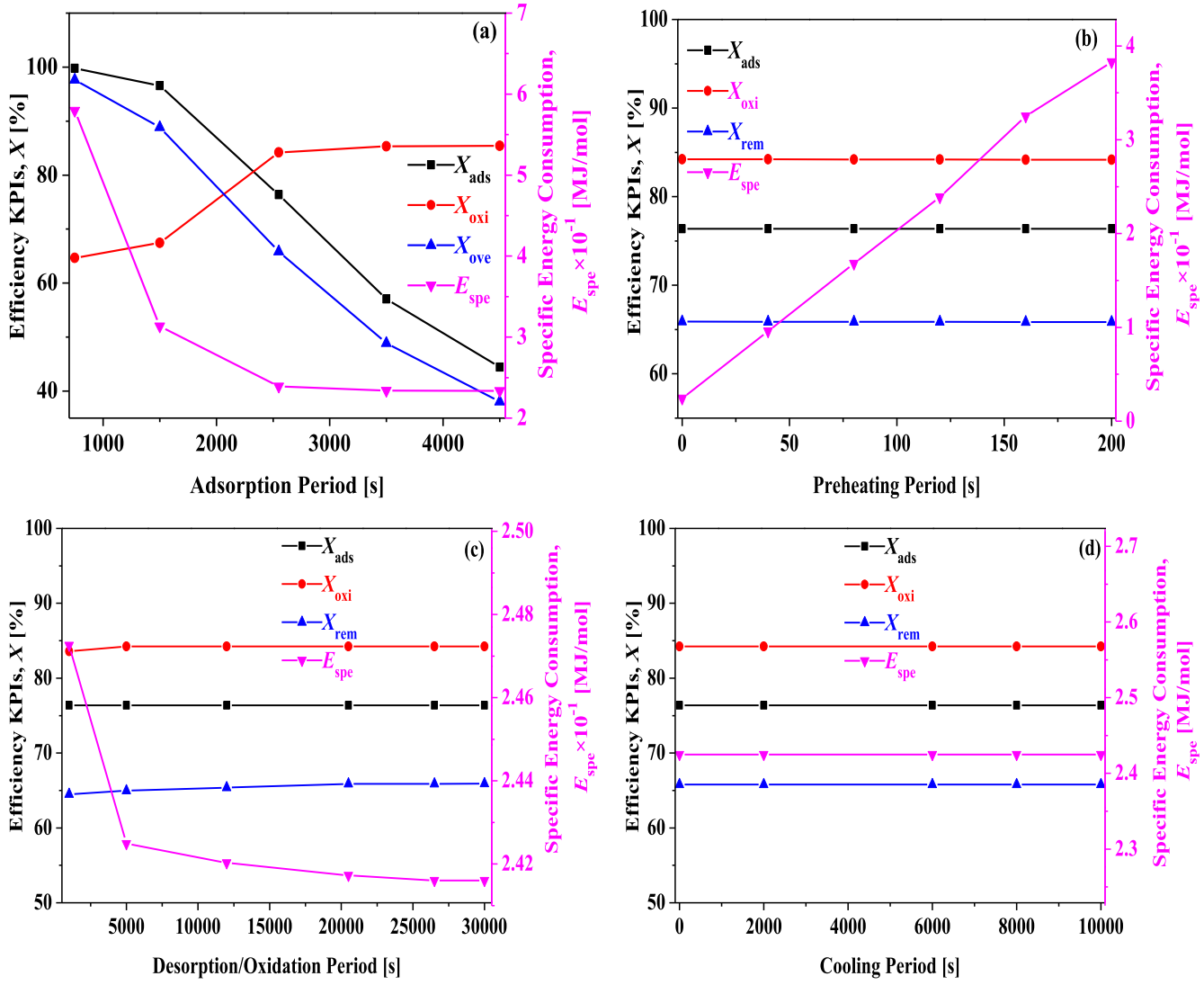

Fig. 11. Effects of (a) adsorption step period (t_{ads}), (b) preheating step period (t_{pht}), and (c) desorption/oxidation step period (t_{deo}) on the KPIs. Bed initial condition: Ar-saturated at 25 °C and 1 atm; adsorptive feed: 50 ppm_v VOC, 25 °C, 1 atm and 100 mL/min; regenerative feed: 21%/79% O_2/N_2, 25 °C initial temperature, 1 atm and 5 mL/min.

of 85.5%. On the contrary, the specific energy consumption decreased gradually from 540 MJ/mol at 750 s to 230 MJ/mol at 2550 s. These observations can be explained by considering the fact that more VOC exited the bed upon increasing adsorption duration, leading to the reduced adsorption and removal efficiencies. Moreover, at longer adsorption step periods, the bed became more saturated, thereby exiting more of the desorbed VOC at the onset of regeneration before the attainment of the light-off temperature (i.e., the temperature at which the oxidation reaction becomes autothermally self-sustainable) (Campesi et al., 2012). The residence time for the desorbed VOC to react with O_2 was greater when it adsorbed nearer the reactor entrance, i.e., the end where the oxidant feed enters. Thus, operation without VOC runaway is desirable for effective TSAO performance and this translates to working in regions of partial adsorbent saturation along the length of the reactor. With increasing adsorption step time, the amount adsorbed increased, leading to increased energy consumption for regeneration. Under identical conditions, the amount desorbed at the longer adsorption step time was high because the amount adsorbed was high, hence the specific energy consumption was reduced. To achieve low specific energy consumption with high-efficiency KPIs, the adsorption period was set to 2550 s corresponding with adsorption, oxidation and removal efficiencies and the specific energy consumption values of 76.4%, 84.2%, and 65.9%, and 23.9 MJ/mol, respectively. Fig. 11b shows that the adsorption, oxidation and removal efficiencies were each constant with preheating period at 76.4, 84.2, and 65.9% respectively. The specific energy consumption, however, steadily increased as heat requirement is a direct function of heating period. However, the amount adsorbed was constant, hence the specific energy consumption increased. Since the efficiency KPIs were independent of the preheating period even as the specific energy consumption increased, then it is conclusive that the specific energy consumption should be as low as possible. This therefore suggests that the preheating step could be neglected which could serve as an advantage by reducing operating cost. Of course, this is reasonable since heating was still continuous even in the desorption/oxidation step. At t_{pht} = 0 s, the values of adsorption, oxidation and removal efficiencies, as well as specific energy consumption were found to be 76.4%, 84.2%, 65.9%, and 2.42 MJ/mol, respectively. As evident from Fig. 11c, all three efficiency KPIs remained unchanged with step time, while the specific energy consumption experienced a sharp between 1000 and 5000 s followed by a gradual decline afterwards. As the effects of the desorption/oxidation period on the efficiency KPIs are insignificant, then the desorption/oxidation period should be set as small as possible to reduce the specific energy consumption, and thus was set at 5000 s. The corresponding specific energy consumption value was 2.42 MJ/mol. As shown in Fig. 11d, the cooling step time had no apparent impact on all the KPIs, on the basis of their definitions (i.e., Eqs. (12–15)). The values of the adsorption, oxidation and removal efficiencies and the specific energy consumption were constant at 76.4%, 84.2%, 65.9%, and 2.42 MJ/mol, respectively. This of course was expected as there was zero energy input to the column during cooling. Based on this, it was concluded that the time required to cool the bed to the adsorption temperature would only be dictated by cooling feed flow rate and/or natural convection.

3.4.5. Investigation of cooling step characteristics

Once the bed is completely regenerated, it must be cooled to the adsorption temperature to start another cycle of the process. To establish a suitable cooling strategy for our combined TSAO process, we considered two approaches, namely, direct and indirect cooling. For the direct cooling contribution, pure Ar gas was continuously and co-currently passed through the bed, while for the indirect contribution, the furnace was opened to the laboratory conditions (~25 °C and 1 atm) to speed up cooling via natural convection with the laboratory environment. Cooling feeds are usually set constant at the prevailing ambient temperature, thus the cooling feed in this study was fixed at 25 °C. Moreover, the shortest cooling period required to return the system to the adsorption temperature under feasible cooling feed must be known. Shown in Fig. 12 are the profiles of the DFM particle temperature as a function of cooling period and feed flow rate at the bed exit and the center of the particle. From these temperature profiles, it is obvious that the cooling time was not affected by the cooling feed velocity. Thus, it is conclusive that the indirect convective cooling rate is far much higher than the direct feed cooling rate, and thus solely responsible for the cooling. Moreover, across all the velocity values, a cooling period of ~2000 s was found to be sufficient to return the system to adsorption temperature of 25 °C.

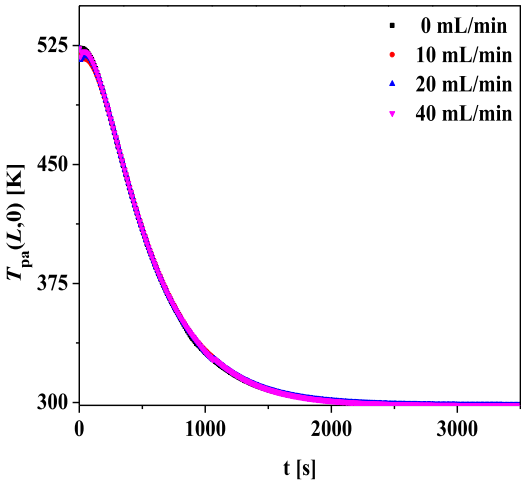

Fig. 12. Bed-exit particle center temperature profile as a function of the cooling feed flow rate ($\dot{v}_{f,cool}$). Bed initial condition: Ar-saturated at 25 °C and 1 atm; adsorption feed: 50 ppm_v VOC, 25 °C, 1 atm and 100 mL/min; regeneration feed: 21%/79% O_2/N_2, 25 °C initial temperature, 1 atm and 5 mL/min; cooling feed: pure Ar at 25 °C, 1 atm and 10 mL/min; adsorption period of 2550 s, preheating period of 0 s, and desorption/oxidation period of 5000 s.

4. Conclusions

In this work, numerical modeling and simulation of a single-unit, four-step TSAO process for the abatement of benzene emission over an adsorbent-catalyst DFM (Ni/ZrO_2-SiO_2) was investigated. The performance of the TSAO process was defined by adsorption, oxidation and removal efficiencies, as well as specific energy consumption. The effects of several operating conditions including adsorption feed conditions, regeneration feed conditions, and step periods on the process key performance indicators were investigated through parametric analysis. The findings of our numerical model demonstrated reasonably good process predictions, making the model a valid description of the TSAO process. All concentration and temperature profiles were properly fitted, and mass and heat transfer parameters were estimated accordingly. However, raising the temperature and velocity of the regeneration input was found to have a marginal impact on the removal efficiency. The parametric analysis revealed that the process variables are heavily linked with the process performance. For example, it was discovered that decreasing adsorption feed conditions, such as concentration, temperature, velocity, and step time, increases removal efficiency. Similarly, while the adsorption temperature has no effect on the removal effectiveness, increasing the reaction temperature increases the removal efficiency proportionately. Furthermore, our findings demonstrated that a complete

TSAO cycle with only three steps of adsorption, heating/desorption/oxidation, and cooling could be operated. Finally, the findings in this investigation revealed that indirect convective cooling, rather than direct feed cooling, can be used to complete the cooling step.

CRediT authorship contribution statement

Busuyi O. Adebayo: Methodology, software, validation, investigation, writing-original draft. **Fateme Rezaei:** Supervision, Conceptualization, Methodology, Writing – review & editing.

Declaration of Competing Interest

The authors declare that they have no known competing financial interests or personal relationships that could have appeared to influence the work reported in this paper.

Acknowledgments

The authors thank the National Science Foundation (NSF CBET-1802049) for financially supporting this project.

Appendix A. Supplementary material

Supplementary data to this article can be found online at https://doi.org/10.1016/j.ces.2021.117356.

References

Adebayo, B.O., Krishnamurthy, A., Rownaghi, A.A., Rezaei, F., 2020a. Toluene Abatement by Simultaneous Adsorption and Oxidation over Mixed-Metal Oxides. Ind. Eng. Chem. Res. 59 (30), 13762–13772.
Adebayo, B.O., Lawson, S., Rownaghi, A.A., Rezaei, F., 2020b. Analysis of Equilibrium and Dynamic Adsorption of Benzene Vapor over Unimodal and Bimodal Silica-Based Mixed-Metal Oxides. Chem. Eng. J. 396, 125273.
Adebayo, B.O., Newport, K., Yu, H., Rownaghi, A.A., Liang, X., Rezaei, F., 2020c. Atomic Layer Deposited Ni/ZrO_2-SiO_2 for Combined Capture and Oxidation of VOCs. ACS Appl. Mater. Interfaces 12 (35), 39318–39334.
Barresi, A.A., Baldi, G., 1992. Deep Catalytic Oxidation Kinetics of Benzene-Ethenylbenzene Mixtures. Chem. Eng. Sci. 47 (8), 1943–1953.
Bird, R.B., Robert, B., Stewart, W.E., Lightfoot, E.N., 2002. Transport Phenomena. J. Wiley.
Bonjour, J., Chalfen, J.-B., Meunier, F., 2002. Temperature Swing Adsorption Process with Indirect Cooling and Heating. Ind. Eng. Chem. Res. 41 (23), 5802–5811.
Campesi, A., Luzi, C.D., Martínez, O.M., Barreto, G., 2012. Effect of Concentration by Thermal Swing Adsorption on the Catalytic Incineration of VOCs. Int. J. Chem. React. Eng. 10 (A54), 1–22.
Campesi, M.A., Luzi, C.D., Barreto, G.F., Martínez, O.M., 2015. Evaluation of an Adsorption System to Concentrate VOC in Air Streams Prior to Catalytic Incineration. J. Environ. Manage. 154, 216–224.
Casas, N., Schell, J., Joss, L., Mazzotti, M., 2013. A Parametric Study of a PSA Process for Pre-Combustion CO_2 Capture. Sep. Purif. Technol. 104, 183–192.
Delage, F., Pre, P., Le Cloirec, P., 2000. Mass Transfer and Warming during Adsorption of High Concentrations of VOCs on an Activated Carbon Bed: Experimental and Theoretical Analysis. ACS Publ. 34 (22), 4816–4821.
Effendy, S., Xu, C., Farooq, S., 2017. Optimization of a Pressure Swing Adsorption Process for Nitrogen Rejection from Natural Gas. Ind. Eng. Chem. Res. 56 (18), 5417–5431.
Effendy, S., Farooq, S., Ruthven, D.M., 2017. A Rigorous Criterion for Approach to Cyclic Steady-State in PSA Simulations. Chem. Eng. Sci. 160, 313–320.
Gangwal, S.K., Mullins, M.E., Spivey, J.J., Caffrey, P.R., Tichenor, B.A., 1988. Kinetics and Selectivity of Deep Catalytic Oxidation of N-Hexane and Benzene. Appl. Catal. 36, 231.
Gelles, T., Krishnamurthy, A., Adebayo, B., Rownaghi, A., Rezaei, F., 2020. Abatement of Gaseous Volatile Organic Compounds: A Material Perspective. Catal. Today 350, 3–18.
Glueckauf, E., Coates, J.I., 1947. 241. Theory of Chromatography. Part IV. The Influence of Incomplete Equilibrium on the Front Boundary of Chromatograms and on the Effectiveness of Separation. J. Chem. Soc. 0, 1315.
Hosseinzadeh Hejazi, S.A., Estupiñan Perez, L., Rajendran, A., Kuznicki, S., 2017. Cycle Development and Process Optimization of High-Purity Oxygen Production Using Silver-Exchanged Titanosilicates. Ind. Eng. Chem. Res. 56 (19), 5679–5691.
Huang, S., Zhang, C., He, H., 2009. In Situ Adsorption-Catalysis System for the Removal of o-Xylene over an Activated Carbon Supported Pd Catalyst. J. Environ. Sci. 21 (7), 985–990.
Joss, L., Gazzani, M., Mazzotti, M., 2017. Rational Design of Temperature Swing Adsorption Cycles for Post-Combustion CO_2 Capture. Chem. Eng. Sci. 158, 381–394.
Ko, D., Kim, M., Moon, I., Choi, D.-K., 2001. Novel Thermal Swing Adsorption Process with a Cooling Jacket for Benzene-Toluene-p-Xylene Purification. ACS Publ. 40 (22), 4973–4982.
Kolade, M.A., Kogelbauer, A., Alpay, E., 2009. Adsorptive Reactor Technology for VOC Abatement. Chem. Eng. Sci. 64 (6), 1167–1177.
Krishnamurthy, A., Adebayo, B., Gelles, T., Rownaghi, A., Rezaei, F., 2020. Abatement of Gaseous Volatile Organic Compounds: A Process Perspective. Catal. Today 350, 100–119.
Kullavanijaya, E., Trimm, D.L., Cant, N.W., 2000. Adsocat: Adsorption/Catalytic Combustion for VOC and Odour Control. Stud. Surf. Sci. Catal. 130, 569–574.
Lopes, F.V.S., Grande, C.A., Rodrigues, A.E., 2011. Activated Carbon for Hydrogen Purification by Pressure Swing Adsorption: Multicomponent Breakthrough Curves and PSA Performance. Chem. Eng. Sci. 66 (3), 303–317.
Miguel, C.V., Soria, M.A., Mendes, A., Madeira, L.M., 2017. A Sorptive Reactor for CO_2 capture and Conversion to Renewable Methane. Chem. Eng. J. 322, 590–602.
Mitsuma, Y., Ota, Y., Hirose, T., 1998. Performance of Thermal Swing Honeycomb VOC Concentrators. J. Chem. Eng. Japan 31 (3), 482–484.
Ntiamoah, A., Ling, J., Xiao, P., Webley, P.A., Zhai, Y., 2015. CO_2 Capture by Temperature Swing Adsorption: Use of Hot CO_2-Rich Gas for Regeneration. Ind. Eng. Chem. Res. 55, 703–713.
Pai, K.N., Baboolal, J.D., Sharp, D.A., Rajendran, A., 2018. Evaluation of Diamine-Appended Metal-Organic Frameworks for Post-Combustion CO_2 Capture by Vacuum Swing Adsorption. Sep. Purif. Technol. 2019 (211), 540–550.
Process Systems Enterprise, gPROMS. http://www.psenterprise.com/products/gPROMS, 1997-2020.
Rezaei, F., Subramanian, S., Kalyanaraman, J., Lively, R.P., Kawajiri, Y., Realff, M.J., 2014. Modeling of Rapid Temperature Swing Adsorption Using Hollow Fiber Sorbents. Chem. Eng. Sci. 113, 62–76.
Shivaji, G.R., Pascaline, P., Sylvain, G., Laurence, L.C., Pierre, L.C., Olivier, B., Stéphane, D., 2012. Different families of volatile organic compounds pollution control by microporous carbons in temperature swing adsorption processes. Hazardous Materials. 221–222, 242–247.
Shokroo, E.J., Shahcheraghi, M., Farniaei, M., 2014. Study of Feed Temperature Effects on Performance of a Domestic Industrial PSA Plant. Appl. Petrochemical Res. 4 (3), 317–323.
Urbutis, A., Kitrys, S., 2014. Dual Function Adsorbent-Catalyst CuO-CeO_2/NaX for Temperature Swing Oxidation of Benzene, Toluene and Xylene. Cent. Eur. J. Chem. 12 (4), 492–501.
Xiao, G., Xiao, P., Lee, S., Webley, P.A., 2012. CO_2 Capture at Elevated Temperatures by Cyclic Adsorption Processes. RSC Adv. 2 (12), 5291–5297.
Yang, J., Lee, C.H., Chang, J.W., 1997. Separation of Hydrogen Mixtures by a Two-Bed Pressure Swing Adsorption Process Using Zeolite 5A. Ind. Eng. Chem. Res. 36 (7), 2789–2798.